

The Development of a Sampling Hadronic Calorimeter for the sPHENIX Collaboration and the Detection of Event Pile-up at PHENIX

Sebastián Vázquez-Carson

Department of Physics
University of Colorado at Boulder

This honors thesis is submitted for the designation of
Academic Honors

Acknowledgements

I would like to thank my wonderful parents that have supported me in every way possible over the course of my life up until this point — undoubtedly, I would not have come this far with you.

I would also like to thank my advisor Jamie Nagle for giving me an opportunity to work in his lab and then for mentoring me over the course of the past two years — you have been an inspiration and an excellent teacher.

I would like to thank everyone in the Nagle lab to whom I have turned to for help when conducting my research — Darren, Ron, Theo, Javier, Kurt, and Sebastian Seeds. You have spent a great deal of time on me and given me the skills to take the next step in my pursuit of physics.

Finally, I want to thank all my friends with whom I have struggled through my physics undergrad — Bill, Purple, and Kevin. Without you, my education would have been solitary, morose, and I am confident that I would have learned significantly less in my classes.

Abstract

The sPHENIX detector at RHIC will contain an electromagnetic and a hadronic calorimeter used for the detection of particles in jets from heavy ion collisions. The hadronic calorimeter will be composed of layers of steel plates that are alternated with plastic scintillators. Within the scintillator panels, wavelength shifting fiber optic cables are embedded and coupled to silicon photo multipliers (SiPMs). The signal from the SiPMs pass through a preamp that shapes and amplifies the signal before passing it to an analog to digital converter (ADC) from which the energy deposited in the scintillator is determined. The scintillator panels are manufactured with a diffusive coating to improve reflection and increase sensitivity. With the test setup at the University of Colorado at Boulder, I explored the correlation between light uniformity and fiber geometry, fiber cladding, and diffusive coating density.

Many measurements made in Heavy Ion experiments such as PHENIX at RHIC rely on knowledge of the geometrical configuration of the colliding nuclei to describe the evolution of collisions and gain insight into the quark-gluon plasma and the strong nuclear force. As part of this investigation, PHENIX has taken data in 2016 for deuteron on gold collisions at several energies. An acceptable collision frequency is achieved by injecting up to 120 separate bunches each with billions of ions into the storage ring, from which two, separate beams are made to collide. This method has a drawback as there is a chance for multiple pairs of nuclei to collide in a single bunch crossing. Data taken in a double event can not be separated into two independent events and has no clear interpretation. I develop an algorithm to flag multiple interaction events by examining the time dependence of data from the two Beam-Beam Counters – detectors surrounding the beam pipe on opposite ends of the interaction region. The algorithm is tested with data, in which events with double interactions are artificially produced.

Table of contents

List of figures	ix
1 Background	1
1.1 Experimental Motivation	1
1.1.1 Hadronic Calorimeter Development for sPHENIX	3
1.1.2 Event Pile Up Detection for PHENIX	6
1.2 Experimental Goals	7
1.2.1 HCal Development: Optimization of HCAL Scintillator Tile Sensitivity Uniformity for sPHENIX	7
1.2.2 Event Pile-up: Optimization of an Algorithm to Detect Event Multiplicity	9
2 Methods in Developing a Hadronic Calorimeter for sPHENIX	11
2.1 Detection of Hadrons	11
2.2 Energy Deposition	12
2.3 Data Acquisition	15
3 Results from the Development of the Hadronic Calorimeter for sPHENIX	23
3.1 The Impact of Fiber Geometry on the Uniformity of Scintillating Tile Sensitivity	23
3.2 Characterizing the Amount of Light Carried in the Cladding of the WLS Fibers	26
3.3 The Impact of Diffusive Coating Inhomogeneity on the Uniformity of Scintil- lating Panel Sensitivity	28
3.4 Results from the 2016 HCal Prototype Test Beam	30
3.5 Conclusion	31
4 Methods in Developing the Double Event Algorithm for PHENIX	33
4.1 Detecting Double Events	33

4.2	Creating and Characterizing Double Events	34
4.2.1	Charge Mixing	35
4.2.2	BBC PMT Time Mixing	36
4.2.3	Vertex Mixing	37
4.3	Double Event Detection Algorithm	38
5	Results from the Development of the Double Event Detection Algorithm	41
5.1	Removing Double Events	41
5.2	Calculating Double Event Populations as Function of Centrality	43
5.3	Calculating Double Event Populations as Function of Collision Rate	44
5.4	Conclusion	46
	References	49

List of figures

1.1	sPHENIX Event Cross Section	2
1.2	Layout of the Relativistic Heavy Ion Collider	3
1.3	sPHENIX Experiment Cross Section	5
1.4	Multi-Fiber Panel Anisotropy	8
1.5	Single Fiber Panel Response	8
2.1	Electromagnetic and Hadronic Showers	12
2.2	The Quantum Mechanics of Scintillation	16
2.3	Technical Parameters for HCal Scintillating Tiles	17
2.4	Outer HCal Panel Engineering Drawing	18
2.5	Inner HCal Panel Engineering Drawing	19
2.6	Silicon Photomultipliers	20
2.7	SiPM Mounting System	21
2.8	PreAmp Diagram	22
3.1	The Effect of a Change in Fiber Geometry	24
3.2	Configuration of Scintillating Panels in the HCal	25
3.3	The Effect of Cladding Light	27
3.4	The Effect of Diffusive Coating Inhomogeneities	29
3.5	Agreement Between the LED Scans and Test Beam Data	30
4.1	Position of the Beam Beam Counters	34
4.2	Illustration of a Double Event	34
4.3	Centrality Components of an Ultra Central Mixed Event	36
4.4	Mixed Event Time Combination Histogram	37
4.5	Vertex Mixing	38
4.6	Detecting Multiple Charge Weighted Peaks in One Event	39

5.1	Frac Cuts	42
5.2	Using Frac Histograms to Estimate the DE Populations in Data	44
5.3	Double Event Rates Across Centrality Bin and Collision Frequency	45

Chapter 1

Background

1.1 Experimental Motivation

Discerning the origins of the universe and its early evolution is one of the fundamental questions in modern physics. The universe, during the first few microseconds after the big bang, was hot and dense enough to forbid the confinement of quarks and gluons in baryonic states of matter. It is believed that during these first few microseconds, all the matter in the universe was a Quark Gluon Plasma (QGP) - a fluid of deconfined, strongly coupled quarks and gluons that only exists under extreme temperature and density. By creating and studying the QGP we gain knowledge of not only the strong nuclear force, but also the earliest stages of the universe that the Standard Model is able to characterize. We can create tiny droplets of QGP in an experimental setting by accelerating nuclei to relativistic energies and colliding them. The high energy density combined with the extreme momenta of the interacting particles at the instant that the nuclei collide allows the interacting quarks to deconfine temporarily. Once deconfined, the characteristic wavelength of the quarks and gluons involved is much longer than the average interaction length of these particles. Because of this, the system must be considered to evolve hydrodynamically as a system of fields and waves, rather than a system of elastically scattering particles. An illustration of the creation and evolution of the QGP is shown in Figure 1.1.

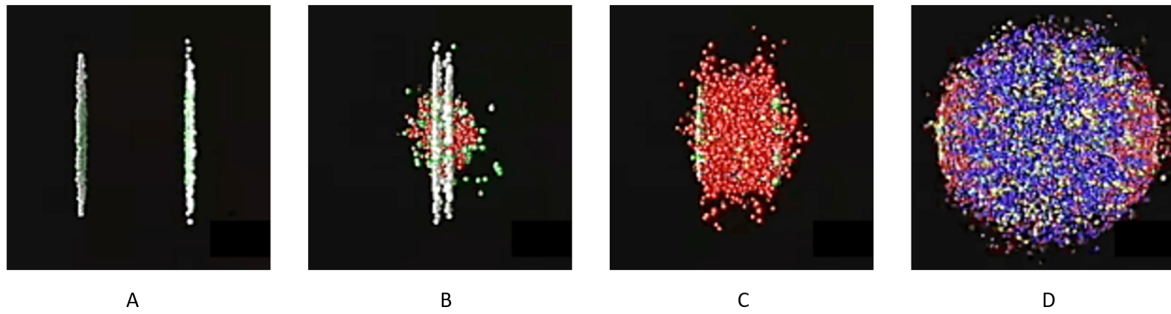


Fig. 1.1 A) Two accelerated, Lorentz contracted nuclei pre-collision. B) The first set of nucleons begin to interact. C) The interacting nucleons melt apart and the interaction length of the quarks and gluons shrinks smaller than a *fermi*, a QGP is created with a radius of 20 fm. D) The QGP evolves hydrodynamically until hadronization [12].

The volume of QGP made in these collisions is extremely small and so we must rely on indirect probes of the deconfined quarks to perturb the medium on our behalf. These perturbative probes include partonic jets created by a hard scattering of quarks and direct photons among other more sophisticated probes. By positioning our detector surrounding the collision region, we are able to observe the final evolution of the QGP long after the quarks have rehadronized we infer the motion of this medium by varying the collision energy, species, and centrality. However, making these measurements requires both constructing a sensitive enough detector to observe the phenomena of interests and translating the data acquired with the detector into key physical quantities — such as final state particle distributions - that characterize a single collision. The layout of the RHIC accelerator complex is shown in Figure 1.2.

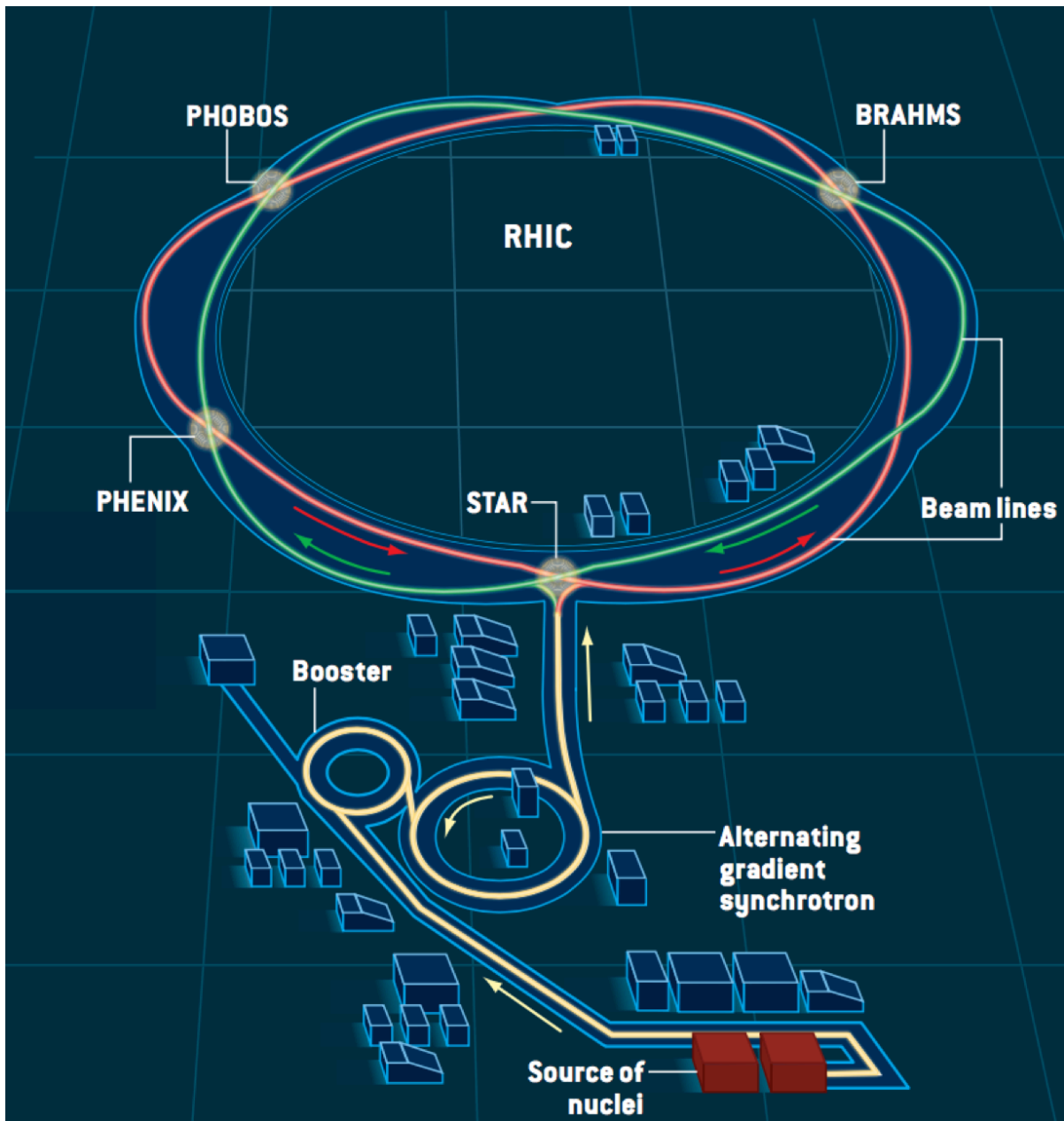


Fig. 1.2 A map of the RHIC accelerator complex with the locations of the experiments highlighted [16].

1.1.1 Hadronic Calorimeter Development for sPHENIX

The 2015 US Nuclear Science Long Range Plan strongly supports the development and construction of a “state-of-the-art jet detector at RHIC, called sPHENIX” [8].

In the collision we have many quarks and gluons scattering that create the QGP. Occasionally, two quarks can scatter with a very large energy transfer. By momentum conservation, these two quarks race in the opposite direction in the transverse plane through the QGP. These high energy quarks interact with the QGP, they then punch out of the plasma. Once outside they fragment in to multiple quarks and gluons which then must hadronize. The resulting hadrons tend to be clustered in an angular cone, referred to as a jet. Knowledge of the total energy of a jet is necessary to fully characterize a collision. Thus, we require a large, dense detector that fully encapsulates the interaction region which is capable of stopping high energy hadrons. Reconstructed jets created at RHIC probe the QGP in the high temperature, strongly coupled regime. A detailed analysis of jet signals will explore energy loss inside the medium – shedding light on the color screening effect and the quark flavor dependence of momentum and radiation losses. However, jets only shed light on the QGP across one length scale. sPHENIX will also probe the QGP on a different scale by studying the sequential melting of the heavy meson upsilon states $b\bar{b}$: $\Upsilon(1S)$, $\Upsilon(2S)$, and $\Upsilon(3S)$ [3]. The aim is that, by working in conjunction with the LHC, we may be able to advance in our understanding of the QGP across a wide range of energies and collision systems from the GeV to the TeV scale. The sPHENIX detector will replace the PHENIX detector on RHIC and will be taking data by 2022 [4]. This will be the first detector at RHIC to utilize hadronic calorimetry for full jet reconstruction at mid-rapidity. The sPHENIX detector will be composed of a set of tracking detectors surrounded by an electromagnetic calorimeter and two hadronic calorimeters inside of a 1.5 T magnetic field. The hadronic calorimeter is a sampling calorimeter, which will be split into two radial segments - one inside the magnet and the other outside the magnet. Accurate jet measurements require coverage over the largest possible solid angle with a minimal inactive area [15]. In total, the detector will provide coverage for $|\eta| < 1.1$ in pseudorapidity [1] as seen in Figure 1.3.

This pseudorapidity acceptance range gives the experiment full azimuthal coverage which permits the reconstruction of high (transverse momentum) jets. The HCal detectors will be constructed with alternating panels of plastic scintillator and steel. As the hadrons ejected in jets from a heavy ion collision pass through the steel, they initiate a shower of muons, pions, and a variety of other particles [14]. These particles then pass through the scintillator, losing energy to scintillating molecules which reemit the light at a longer wavelength which is then collected by embedded fiber optic cables. The light trapped in the fibers is projected onto a SiPM (solid state Silicon Photomultiplier), digitizing the signal.

In the following sections, I describe the process of testing and developing various components of the Inner and Outer HCal's – including, plastic scintillator tiles, various fiber optic

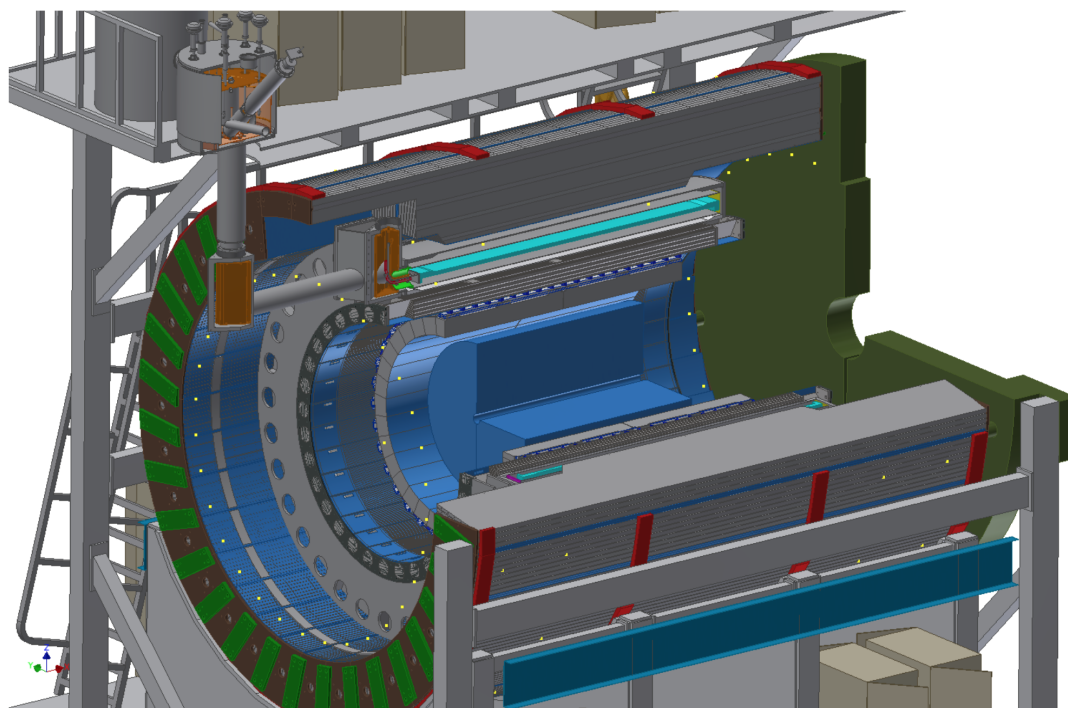


Fig. 1.3 A cross section of the sPHENIX upgrade on the existing support for PHENIX. Collisions occur in the center of the detector pass through the tracking detectors, electromagnetic calorimeter, and inner hadronic calorimeter (all shown in blue) before passing into the outer hadronic calorimeter (shown in green) [4].

cables, SiPMs, and signal processing electronics. Additionally, I will analyze the effect manufacturing inconsistencies have on spatial signal clarity and propose several improvements that could be made. Finally, I will give a synopsis of the data taken in March and April of 2016, when the sPHENIX prototype was tested at Fermilab using their test beam facilities.

1.1.2 Event Pile Up Detection for PHENIX

Many measurements made in heavy ion experiments such as collective flow that give insight into the properties of the quark-gluon plasma depend on the geometrical configuration of the colliding nuclei. As part of this investigation, the PHENIX experiment at the Relativistic Heavy Ion Collider has taken data in 2016 for d+Au (deuteron on gold) collisions at $\sqrt{s_{NN}} = 200\text{GeV}$. Events are created by injecting up to 120 separate bunches each with billions of ions into the storage ring, from which two, separate beams are made to collide. This introduces the possibility for multiple nuclei to collide in one bunch crossing. When two separate pairs of nuclei collide in the same bunch crossing, it is called a double event; the phenomenon of multiple interactions per bunch crossing is collectively called event pileup. Data taken in a double event cannot be separated into two independent events and has no clear interpretation because the detectors have no way of discerning particles released in the primary event from particles propagating from the secondary event. The extent of the event pile up problem is heavily dependent on the collision system in question and is proportional to the total number of nuclei in each ion bunch. Therefore, the statistical removal of double events is necessary for small collision systems with low multiplicity such as p+Al or d,3He + Au.

While many modern high energy physics experiments have a solid-state vertex detector surrounding the interaction region of a collider, the PHENIX experiments' vertex detector performance has declined significantly after 5 years due to radiation damage. This has eliminated the detector's ability to detect event pile up in the later runs, so other double event detection methods must be explored while sPHENIX is in development.

I developed several additional algorithms to flag events with multiple interactions by examining the time dependence of data from the two Beam-Beam Counters – detectors surrounding the beam pipe on opposite ends of the interaction region. The algorithms were tested with data, in which events with double interactions are artificially produced using low luminosity data.

1.2 Experimental Goals

1.2.1 HCal Development: Optimization of HCal Scintillator Tile Sensitivity Uniformity for sPHENIX

sPHENIX will require a jet energy resolution of $\sigma/E < 120\%/\sqrt{E}$ which corresponds to an energy resolution per hadron in the full calorimeter system of $\sigma/E < 100\%/\sqrt{E}$. To acquire accurate data concerning collisions, it is essential to create a uniform light response across the entire panel with the highest energy capture possible. Regions on the tile with increased sensitivity will report the deposition of a greater amount of energy than less sensitive regions. The reconstruction of event jet energies recorded with the HCal relies on the fact that the repeated detector segments are all as identical as possible to consistently translate light deposited in the panel to total energy carried by the hadron detected. We test the effects of a diffusive coating variation, fiber placement, and multiple energy deposition methods on the uniformity of a panel's light response. First I examined the effect that various fiber placements had on recorded tile sensitivity. The sPHENIX HCal, will use wavelength shifting (WLS) fiber optic cables embedded in the scintillator tiles to collect the light generated by hadronic showers and change its wavelength to 490 nm to which our SiPMs are sensitive. Previous work done by Sebastian Seeds of the Nagle lab showed that fiber positioning is of critical importance to panel light uniformity [13]. Additionally, I investigated the effect fiber cladding had on response uniformity with the aim of explaining certain observed light asymmetries on the tiles.

Next I wanted to determine if I could use 405 nm LED pulses to deposit energy in the panel rather than β radiation from a Sr 90 source. This was motivated by the shift in panel design to incorporate one SiPM per panel which significantly lowered the cost of assembling the full detector and halved the amount of data that would need to be analysed per event. However, this eliminated the possibility of triggering the data acquisition on a double coincidence between two SiPMs which is required to use the Sr 90 source. LED's offer the advantage of extremely fast event simulation using the LED as an extremely accurate trigger with energy deposition occurring at the MHz range rather than the kHz range of the Sr 90 or the Hz range of cosmic rays.

Finally, I examined the effects of inconsistencies in the diffusive coating application and panel thickness inconsistencies from the plastic extrusion process during mass-production. These measurements aimed to identify areas where the highest level of quality control was necessary, and components that did not require this attention to detail.

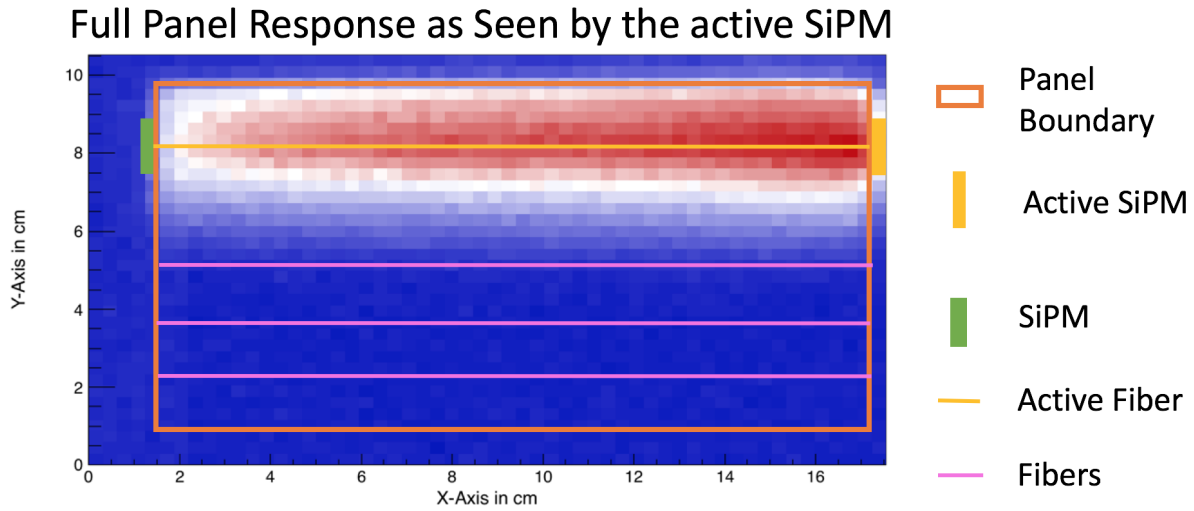


Fig. 1.4 A multi-fiber scintillator panel scan using β radiation and a double coincidence trigger from two SiPMs. Note the response anisotropy and the response gradient along the fiber. In this plot, red indicates a higher response and blue shows areas with little to no response.

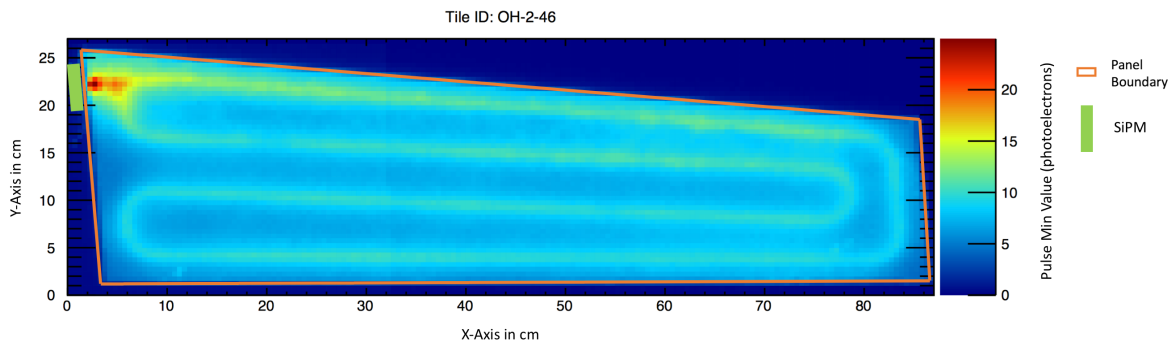


Fig. 1.5 The finalized panel design with one SiPM, one long fiber, and a much more uniform signal across the panel. Again, red indicates a region with a higher light sensitivity, while dark blue shows areas with no sensitivity.

1.2.2 Event Pile-up: Optimization of an Algorithm to Detect Event Multiplicity

When constructing the event pile up detection algorithm, I intended on creating an algorithm that would take in data recorded using PHENIX and cut out data containing multiple events. The idea of inspecting the timing distribution of spectator ions using the BBCs (beam-beam counters) at opposite ends of the detector along the beam was initially developed by one of our PHENIX collaborators, the Rosati Group at Iowa State. However, I needed to improve Qiao's (Vanderbilt University) algorithm because it was not distinguishing between double events and single events with a high enough purity. Therefore, my aim in constructing the algorithm was to use BBC data to cut out double events from the data with the highest accuracy possible and to investigate any biases introduced in the events passing the cut.

Chapter 2

Methods in Developing a Hadronic Calorimeter for sPHENIX

2.1 Detection of Hadrons

Charged hadrons (π^\pm , K^\pm , p , \bar{p}) primarily lose energy through the ionization of the medium they are passing through for low momenta. However, higher energy hadrons (charged and neutral) can interact through the strong force with nuclei. An exchanged virtual boson (photons, gluons, W^\pm , Z^0) decays into other hadrons or leptons, which continue to interact and perpetuate the shower. Due to the relatively long mean distance between interactions, hadronic calorimeters must be significantly larger than their electromagnetic counterparts. For example, the nuclear interaction length of iron $\lambda_I = 17$ cm is significantly longer than its radiation length $X_0 = 1.8$ cm [14]. Hadronic showers can even give rise to electromagnetic showers through the decay of $\pi^0 \rightarrow \gamma\gamma$. Up to 30% of the energy of a hadronic shower goes into nuclear excitation and other processes and is undetectable using our methods. Therefore, it is essential to calibrate the detector using particles with a known energy so that the efficiency of the calorimeter can be measured and compensated for [14].

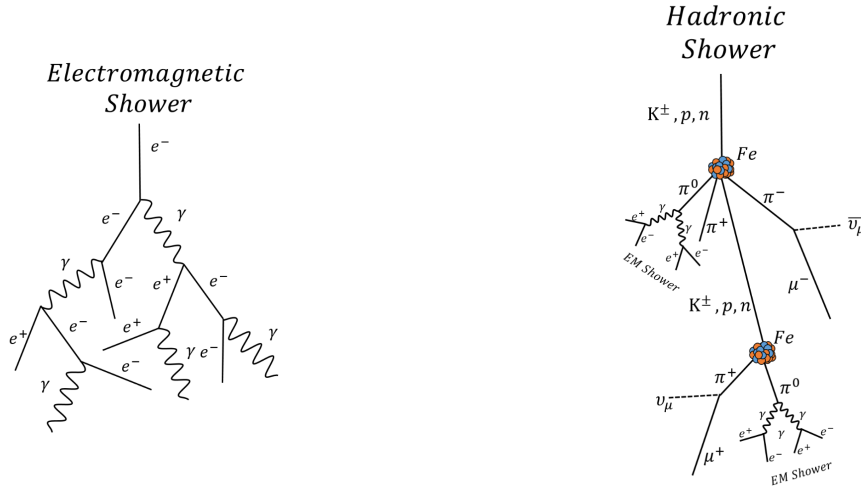


Fig. 2.1 Schematic of an example electromagnetic shower (left) and hadronic shower (right).

2.2 Energy Deposition

Energy was initially deposited in the scintillating tiles using a collimated Strontium-90 β^- source attached to two stepper motors in x and y. The Strontium-90 β^- source was eventually replaced with a collimated 405 nm LED.

Energy Deposition Method One: Sr 90 Source

When sPHENIX is taking data, energy will be deposited through hadronic showers initiated by high energy hadrons. The most consistent, realistic way to simulate this is to use a radioactive source to shower particles onto the panel. When Strontium-90 decays to Yttrium-90, it releases β^- radiation at 0.546 MeV, which provides sufficient energy to test the panel.



The Strontium-90 source we use is kept in a solid brass housing that prevents the source from showering particles in all directions. Down the lower half of the cylinder's axis, a 1 mm aperture was milled to direct the stream of e^- down, directly away from the source. This is all attached to the stepper motors, by which we can aim the radiation at any discrete position in the light tight test stand. The primary drawbacks of the β^- radiation method is that data taken with this source is reliant on a double coincidence trigger, which becomes impossible if your

scintillating panel only has one SiPM (silicon photomultiplier). Additionally, the β^- radiation provided by this source is only at 0.546 MeV while the highest energy particles ejected in collisions can have up to 50 GeV [10].

Energy Deposition Method Two: 405 nm LED Light

High energy hadrons passing through the scintillator electromagnetically scatter off the scintillating molecule's electron clouds. Therefore, one should be able to deposit energy in the panel directly using photons - the exchange boson of the electromagnetic force.

I milled a new collimator out of brass that was functionally identical to the one used to insulate the β^- source, but the inside of the collimator was equipped with a mounting system for an 405 nm LED. This LED was collimated to a similar degree as the beta source and placed in the stepper motor housing. From this position, the LED can be made to scan tiles as with the β^- source, but our data acquisition can be triggered directly from the LED's power supply. This eliminates the need for a double coincidence, allowing the experiment to function with only one SiPM, as opposed to two. This vastly simplifies the analysis of data taken with the test stand and improves the frequency of data acquisition from 0.02 Hz into the 1 MHz range. Unfortunately, 405 nm light is not particularly high in energy, therefore this method is not capable of testing the HCal's performance at the maximum operational energies.

Energy Deposition Method Three: Cosmic Rays

Cosmic rays are an accessible, excellent source of high energy particles that can be used to characterize the scintillating panel's response in the high energy limit. Cosmic rays are primarily a high energy protons- however, electrons and more exotic particles can also be cosmic rays. [11] These high energy particles are accelerated to relativistic energies of 10^5 GeV [9] by supernova shock waves. When these particles strike Earth's upper atmosphere, they initiate a hadronic shower. Muons are the longest traveling particles produced and are the primary source of detected cosmic ray energy in the scintillating tiles we tested. The characteristic spectrum of cosmic is very well known, so cosmic provide the ideal test for determining the energy sampling fraction of the panels. Unfortunately, we rely on two PMTs (Photomultiplier Tubes) positioned above and below the panel to provide the double coincidence we require to trigger the data acquisition. Additionally, the flux of cosmic rays is low enough that for a 1 cm^2 PMT trigger, one sees approximately only one cosmic per minute (0.02 Hz) making this a very slow method of taking data.

Light Insulation

Due to the sensitivity of my experiment to visible light, all data was taken inside of a light tight box in the Nagle lab's facilities at CU Boulder. The previous research of S. Seeds on the properties of the SiPMs and scintillating panels was conducted using a scaled down version of the light tight box I used. Therefore my first task was to construct a larger test stand capable of accommodating tiles of up to 1.5 meters in length. The test stand was scaled up from a box of dimensions $86 \times 86 \times 124 \text{ cm}^3$ to one of dimensions $90 \times 120 \times 180 \text{ cm}^3$. This required installing scaled up stepper motors to move the source, cutting and constructing a new panel and motor support framework out of 80/20 aluminum, and editing some basic aspects of the motor actuator code. The construction of the support framework out of 80/20 aluminum provided a great deal of flexibility regarding mounting of test panels and external triggers—such as PMTs for cosmic triggers. Cables were permitted to access the inside of the box to provide power and collect data via a junction on one side where cables could be plugged into either side—transmitting data without compromising the test stand. Due to the low operating voltages of the SiPMs implemented, there was no need to install an interlock to shut down the equipment if the box was accidentally opened while in operation. The test stand was locked shut securely during all data acquisition.

Moving the Sources: The Stepper Motor Program

The aim of my experiment is to provide a spatial map of the sensitivity of the scintillating panels being investigated; as such, a consistent way to move the Strontium-90 source across the full surface of the panel is required. By placing two orthogonal stepper motors on rails above the panels being tested, I was able to acquire a full range of motion in the X, Y plane: $X \in (0, 150)$ cm and $Y \in (0, 100)$ cm.

The stepper motors are controlled via C++ code written by S. Seeds of the Nagle Lab and improved by me. This macro utilizes functions written by the motors' manufacturer and is run through the terminal of the computer that operates the rest of the DAQ (Data Acquisition) and commands are transferred via USB to the motors themselves. Each motor has a discrete number of steps within its range, which can be set in each iteration of a for loop. By changing the number of discrete positions I sent the motors to, I was able to control the resolution of my scans. When conducting a scan, I choose the number of steps in X and Y while simultaneously specifying the amount of data I desire to be taken at each position. The resolution of the scans

had an upper bound corresponding to the size of the collimated beam of β^- ($\approx 1 \text{ mm}^3$) and LED light ($\approx 10 \text{ mm}^3$). The error in X and Y for each stepper motor is $\pm 1 \text{ }\mu\text{m}$.

2.3 Data Acquisition

The data acquisition converts momentum carried by hadrons into a text file that can be analyzed later. Scintillating panels convert kinetic energy carried by a hadronic shower into ultraviolet light. The scintillating tiles are coated with a diffusive powder that improves the tile's internal reflection, giving the light deposited by hadrons a better chance of getting into the embedded wavelength shifting (WLS) fiber optic cable. The light travels along the WLS cable and is deposited on an SiPM, which releases a discrete amount current per pixel hit by the light. This signal is passed to a preamp designed by S. Boose of the PHENIX collaboration that shapes the signal into a smooth pulse and amplifies it. The data then travels via coaxial cable to a logic module that can be programmed to complete logical tasks such as: requiring up to four signal coincidences, delaying signals, and filtering small sources of noise. The data is finally recorded using an oscilloscope and can be triggered from the coincidence module or the LED's power supply. Initially, the integral of the signal from the scintillating panels was recorded, but later experiments record the magnitude of the signal pulse in the interest of faster data recording. Finally, these values are sent to the computer that runs the oscilloscope and stepper motors, where the data is recorded in a text file that can be exported for analysis.

Plastic Scintillating Panels

A scintillator is a substance that absorbs some of the momentum of a particle passing through it and emits the energy deposited as light. As charged particles interact with the electrons of the scintillating molecules, they dissipate energy to the electrons which after some time in an excited state, release a photon and decay into a more stable state. The emission process is called fluorescence, while the entire process of excitation, emission, and photon propagation are referred to as scintillation. The scintillating molecules are mixed in with an optically transparent polystyrene and this mixture is extruded into the panels used in sPHENIX.

The scintillator's electrons begin in the $S_{0,0}$ state, which is the lowest vibrational state of the ground electron state. [13] Passing charged particles that are created in hadronic showers interact electromagnetically and excite the scintillating electrons. Electrons excited into higher vibrational modes, $S_{1,N}$ ($N = 1, 2, 3, \dots$) dissipate vibrational energy to the electrons near them

and create a population of excited electrons $S_{1,0}$ across a single molecule. After some characteristic decay time τ_f , which is dependent on the scintillating molecule in use, the electrons in the $S_{1,0}$ state decay back to the vibrational ground state, $S_{0,0}$, and fluoresce.

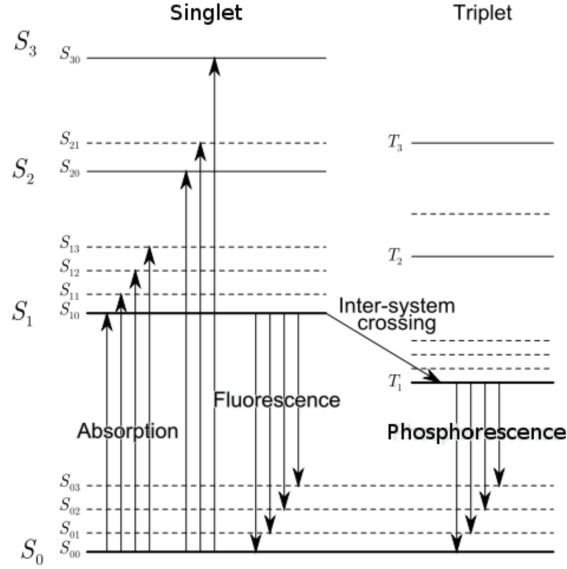


Fig. 2.2 The possible excited state transitions for the scintillating molecules— S_N are the vibrational states of the molecule [7].

This fluorescence is characterized by [7]

$$I = I_0 e^{-t/\tau_f}. \quad (2.2)$$

In addition to vibrational modes, electrons can be excited into an *optical state*, where the electron is excited into a more energetic state than the other electrons on the same atom. In scintillators with a very short relaxation time, the number of photons emitted in a single light pulse is given by [7]

$$N = \alpha^{-t/\tau_f} + \beta^{-t/\tau_s}, \quad (2.3)$$

where τ_s is the characteristic lifetime of the optical state. In fast scintillators, such as the ones used in sPHENIX HCAL, $\tau_s \approx 0.5$ ns and $\tau_f \approx 2$ ns. In total these effects give a light pulse with a time dependent intensity [13]

$$I = I_0 f(t) e^{-t/\tau_f}, \quad (2.4)$$

where $f(t)$ is a Gaussian. The fluorescence process is dependent on the vibrational fine structure of the molecule. This vibrational fine structure is dependent on the internal energy of the scintillating solid, therefore the intensity of light emitted in the panel is closely tied to the ambient temperature. The sensitivity of the SiPM is also affected by temperature variations. The experiment was held at constant temperature and a thermistor was included in the circuit that powers the SiPM to account for these effects.

Property	
Plastic	Extruded polystyrene
Scintillation dopant	1.5% of PTP and 0.01% POPOP
Reflective coating	Proprietary coating by surface exposure to aromatic solvents
Reflective layer thickness	50 μm
Wrapping	100 μm Al foil followed by one layer of 30 μm cling-wrap and a 100 μm layer of black vinyl tape
Attenuation length in lateral direction (with respect to extrusion)	≈ 3 cm
Wavelength shifting fiber Formulation	Single clad Kuraray Y11 200, K-27, S-Type
Cladding material	Polymethylmethacrylate (PMMA)
Fiber diameter	1 mm
Emission peak	476 nm
Fiber core attenuation length	> 200 cm
Optical cement	EPO-TEK 3015

[H] Fig. 2.3 Technical Parameters for HCal Scintillating Tiles [15]

There are two primary panel designs that are being utilized in the construction of the sPHENIX HCal - one for the inner calorimeter and another for the outer calorimeter. The scintillating dopant used for both panels is identical, as is the diffusive coating compound (see Figure 2.3).

Fiber optic cables collect the light emitted by scintillating molecules in the panels and deposit it on the panel's SiPM. The scintillator used in this experiment fluoresces in the ultraviolet range of the spectrum. Due to the lack of sensitivity of the SiPM to radiation of this wavelength, the fiber optic cables used in the experiment must convert the light emitted by the scintillating molecules into light in the visible spectrum. The fiber placement varies between inner and outer HCal tiles as can be seen in the included panel schematics (Figures 2.4 and 2.5). This fiber variance is necessary to account for the difference in the areas of each panel. The inner HCal

will be closer to the interaction region and can cover the same solid angle with smaller panels; this enables the inner HCal to fit inside the magnet necessary for the tracking detectors.

Due to the limited amount of light deposited in a panel by a hadronic shower, it is essential to collect that light with the greatest possible efficiency. The panels are encased in a $50\ \mu\text{m}$ thick proprietary diffusive coating that improves each panel's internal reflection. The sPHENIX collaboration was not informed of the specific chemical composition of this coating, which is considered a trade secret by the manufacturer. However, the coating is known to be the product of exposing each tile to aromatic solvents.

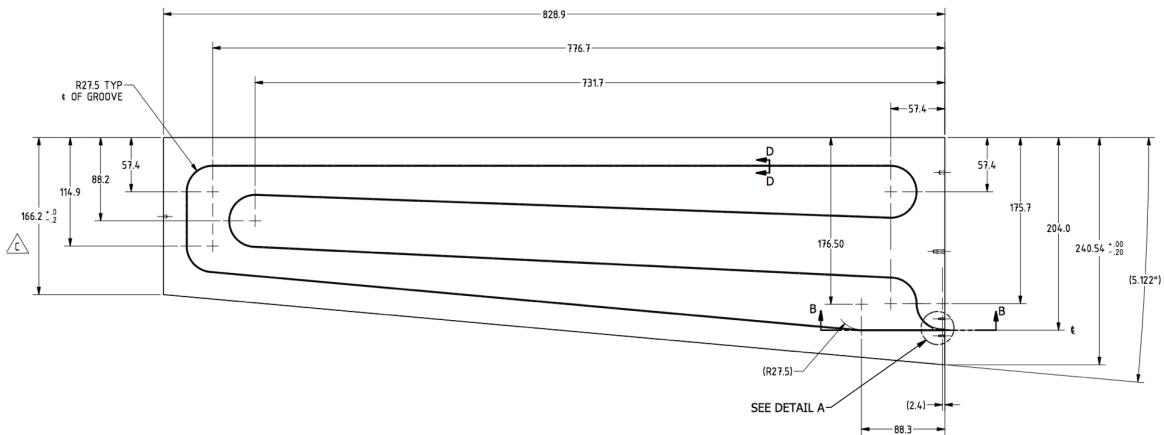


Fig. 2.4 An engineering drawing of an outer HCal panel.

Wavelength Shifting Fibers

Energy deposited in the scintillating panels by hadronic showers is gathered by an embedded 1 mm (diameter) single clad Kuraray Y11 fiber. This fiber is optically coupled to the scintillator panel and glued in place with an optical cement which is transparent to ultraviolet light. This fiber absorbs the light propagating in the panel and emits it with an emission peak of 476 nm. Each panel is oriented with the fiber ends pointing radially outward, where an SiPM digitizes the analogue signal. The sharp turns imposed by the selected fiber geometry cause a great deal of mechanical stress on the fiber. The Kuraray Y11 fiber was selected due to its durability and flexibility [15].

The specific geometry for inner and outer HCal tile fibers was designed such that energy deposited in the panel is always within 2.5 cm of the fiber. The radius of the fiber's turns was limited at 2.5 cm to limit mechanical stress related light loss. The more one bends a fiber optic

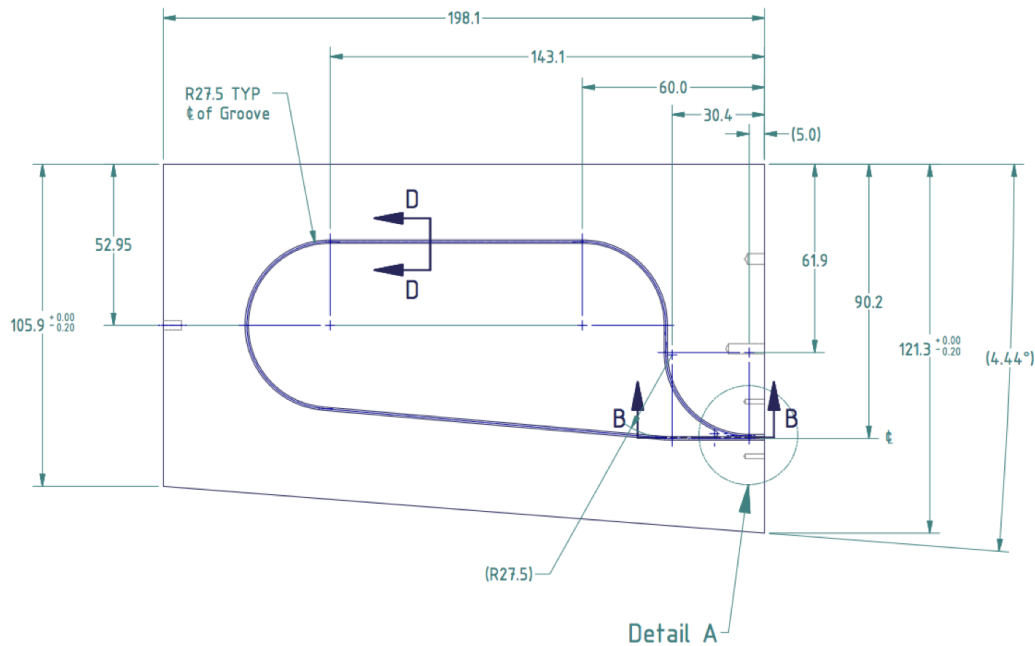


Fig. 2.5 An engineering drawing of an inner HCal panel.

cable, the worse the fiber's internal reflection becomes; therefore keeping the largest radius of curvature possible was an additional constraint on the fiber geometry [15].

Silicon Photomultipliers

Silicon photomultipliers are arrays of thousands of avalanche photo diodes (APD) operating in Geiger mode, attached to a shared silicon base that are used to detect single photons. Previous experiments have used photomultiplier tubes (PMTs) to detect the light in the experiment, but SiPMs offer several distinct advantages over PMTs. SiPMs are considerably smaller than PMTs, making the overall detector smaller and SiPMs are easy replace given that they can be mounted onto the panels directly. Finally, SiPM's require a much lower voltage to collect data than PMT's, which not only is safer for those working on the experiment, but is also cheaper to power because there is no need for expensive kV power supplies.

Photons incident on a pixel of the SiPM are absorbed by the valence electrons of the silicon. These electrons can become ionized, and once ionized, they are accelerated by the supplied voltage of 80 V. As the accelerated electron moves, it ionizes other electrons in the silicon and builds a detectable current. Once the current reaches a critical level, a quenching resistor on the

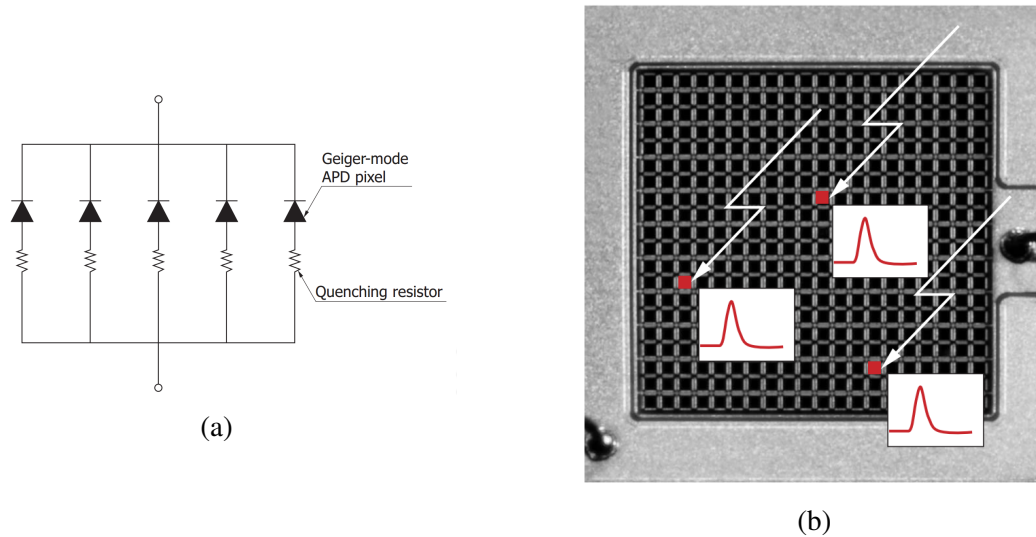


Fig. 2.6 (a) Each pixel has its own quenching resistor, enabling each to record data independently. (b) A magnified image of an SiPM face showing the incident photons and the resulting signal [5].

SiPM lowers the voltage across each pixel and stops the avalanche (Figure 2.6a). The output current from the Geiger discharge is a pulse waveform with a short rise time and the quenching resistor introduces a relatively slow fall time (Figure 2.6b) [5].

The SiPMs used in this experiment have a surface area of 3 mm^3 with 14400 pixels. Constructing each pixel in parallel permits us to detect multiple photon signals independently and add them discretely. We rely on this to calibrate the SiPM because if the SiPM is operating correctly, one should see discrete pulses as different pixels fire. These single photon signals are called photoelectron peaks and the ability to resolve these is proof that the SiPM is functioning correctly.

The SiPMs are attached directly to the side of the panel where the two ends of the WLS fiber are exposed. The fibers are embedded deep enough into the panel so that they project into the middle of the SiPM's face. The SiPM is held a short distance away from the end of the fibers to allow the light in the fiber to cover a larger area of the SiPM. Very luminous signals could fire all the pixels in an area and saturate the SiPM; however, by exposing a large SiPM area, the risk of saturation is minimized. We allow a gap of 0.75 mm between the fiber ends and the SiPM to allow for no greater than a 5% variation in response when the fibers are misaligned by 0.2 mm [15]. I prototyped the initial designs for these mounting brackets using the industrial 3D printer owned by CU's engineering school.

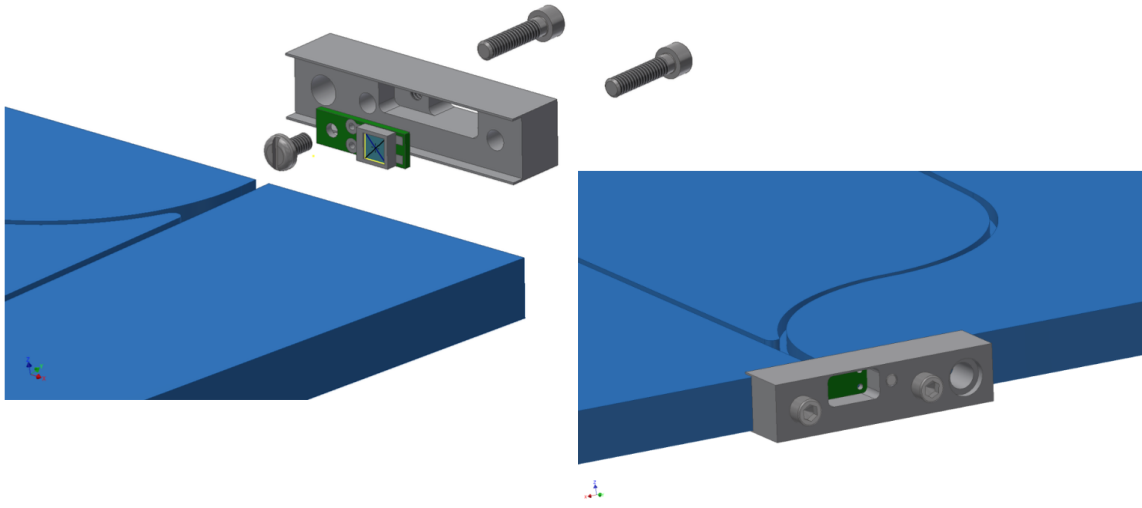


Fig. 2.7 SiPMs are housed in a 3D printed mounting bracket that is screwed into the panel [15].

Readout Electronics

The electronics that smooths the SiPM pulses and amplifies the signal is common between the EMCAL and the two segments of the HCal. In the detector, panels are grouped into sets of five adjacent panels. The preamp passively sums the signals from the five panels and then amplifies them. The input of the amplifier acts as a transresistance amplifier, having a very low input impedance to the SiPMs allows current generated by the SiPMs to flow more freely and improves the signal gain. The preamps have two gain settings corresponding to a normal energy scale and a high energy scale ($g_{\text{high}} = 16 \times g_{\text{normal}}$). Upon amplification, the signal is shaped to have a peaking time of 30 ns for a 60 MHz sampling that is differentially driven to the ADC [15].

Oscilloscope DAQ

After the signal from the SiPM has passed through the preamp circuit, it proceeds to a logic module that can identify double coincidences from multiple SiPMs or PMTs in Sr 90 scans or cosmic scans. The logic module then acts as a trigger for an oscilloscope that records the magnitude of the signal peak from the preamp in mV. The updated fiber geometry only utilizes one SiPM, so triggering on double coincidence in this set up is impossible. In this test configuration, the oscilloscope is triggered directly off of the function generator that powers the LED for these scans. For the sake of clarification, LED scans produced all data taken with the

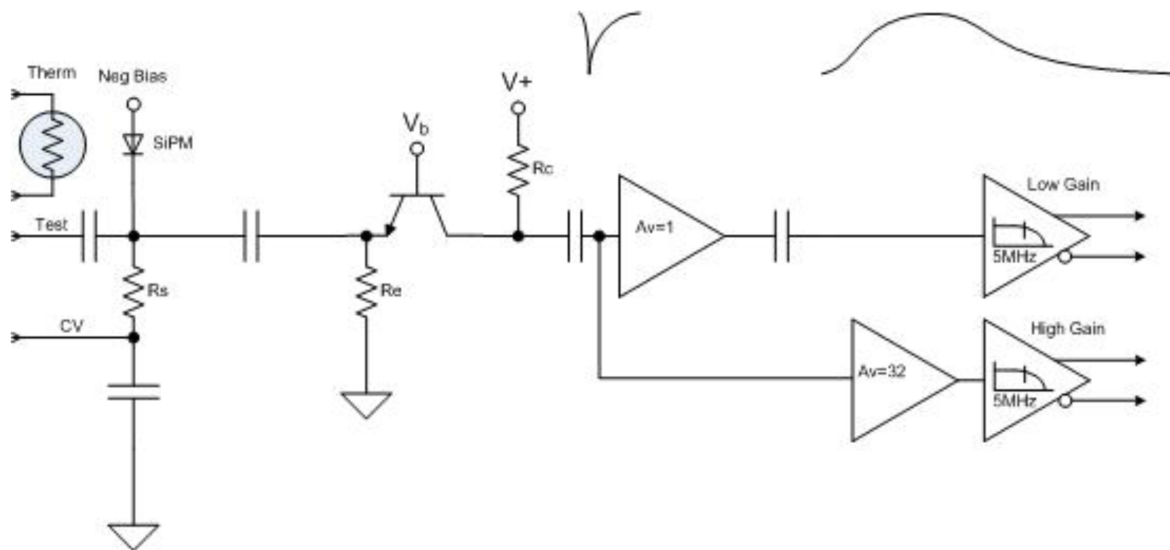


Fig. 2.8 The preamp used for the EMCal and HCal designed by S. Boose of BNL [15].

single fiber geometry panels, but the four fiber panel data was taken with both the Sr 90 and LED sources. Finally, the oscilloscope transmits the magnitude of the signal peak via USB to the test stand's central computer where it is recorded as a text file for later analysis. These text files can be opened and analyzed using any suitable program or language. All of the high level analysis of this data was done using Root, an object oriented C++ library developed by CERN.

Chapter 3

Results from the Development of the Hadronic Calorimeter for sPHENIX

Over the course of these experiments, it has been my goal to optimize the uniformity of the light response from the HCal scintillating tiles. To that end, I found three primary sources of response asymmetry: fiber geometry, light carried in the fiber cladding, and inhomogeneities in the diffusive coating. Having identified these sources, the sPHENIX collaboration has been able to account for these effects to varying degrees and incorporate my observations in the final HCal design. Finally, I will present results from the 2016 Test Beam at Fermi Lab, where we constructed a prototype HCal and tested its performance using a beam of relativistic hadrons.

3.1 The Impact of Fiber Geometry on the Uniformity of Scintillating Tile Sensitivity

Initially, I was investigating light uniformity across small scintillating tiles containing multiple embedded fibers of similar dimensions to the inner HCal tiles as shown in Figure 3.1.b. However, there were several large problems with that design that arose as a direct product of the fiber geometry, namely this design was grossly inefficient. It required eight SiPMs to provide full tile coverage, which is an unacceptable number of SiPMs per tile considering that there will be thousands of such tiles in the sPHENIX experiment. Additionally, by mounting SiPMs on either end of the tile, one introduces a large amount of wiring and circuitry to the interior surface of the HCal. This would introduce a great deal of empty space in the detector, which decreases the amount of space available for the actual detector. It is also highly impractical to take apart

sPHENIX once it is assembled, making the inner surface of the HCals almost impossible to maintain. Finally, adding SiPMs does not only increase the cost of constructing the HCal, it also adds more channels from which data must be recorded and analyzed.

Using tiles with the straight fiber geometry requires multiple SiPMs to provide full panel coverage. If the data from only one of these SiPMs is recorded, a massive asymmetry is introduced into the response of the tile, as shown in Figure 3.1. This figure makes it apparent that the attenuation length of the tiles is short enough that light emitted more than two centimeters from the fiber is much less likely to be seen by the SiPM. The straight fiber tile scan shown in this Figure (3.1.b) reveals that for this fiber geometry, the half of the panel opposite to the fiber is no more sensitive than the air surrounding the panel (the outside boarder of the scan). If one does not employ all the SiPMs in the old tiles, up to half of the tile becomes worthless.

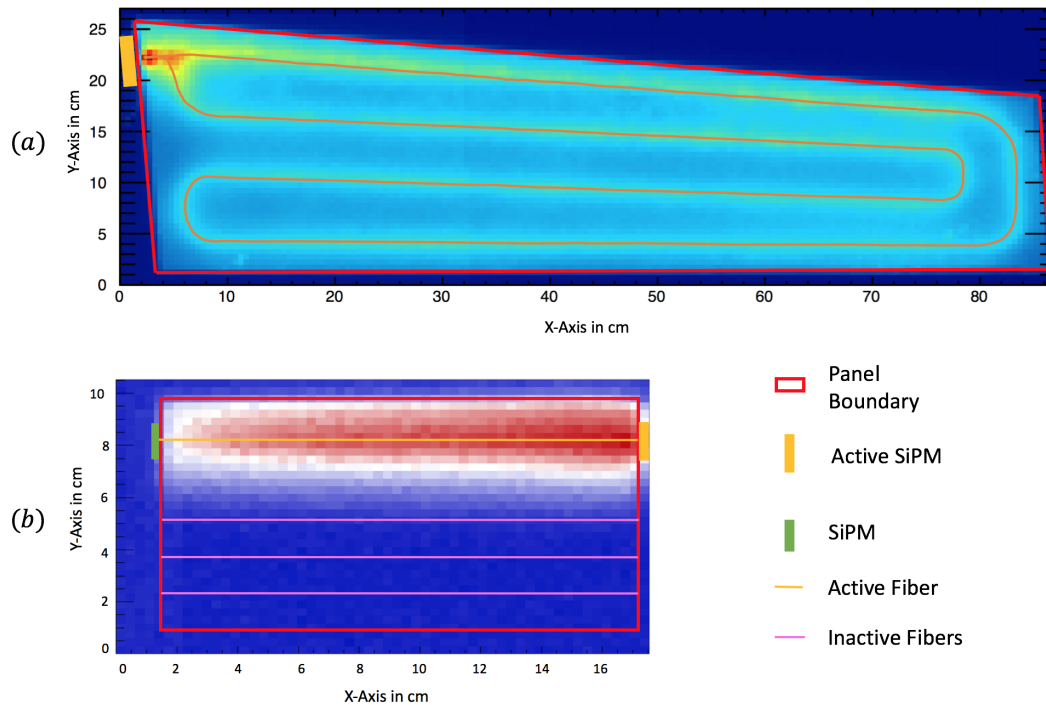


Fig. 3.1 Shown are two different scans of different panels with a variation in their fiber geometries. (a) The new panel with one SiPM a single embedded fiber that provides full coverage over the panel's face. (b) An older panel design that is smaller and has four fibers. This scan was triggered off a double coincidence between two SiPMs attached at opposite ends of the panel, but I only show the signal from the SiPM on the left.

With that in mind, the collaboration decided to switch to the HCal panel designs shown in Figures 2.4 and 2.5 in the HCal methods section (2.3). These panels are slightly more difficult to manufacture due to added complexity in the fiber path that must be milled into the tile, but they offer several major advantages over the simple four-fiber tile design. The new single fiber, single SiPM design is less expensive due to the elimination of seven SiPMs and all of the equipment needed to power them and collect their data. The new panels do not have any SiPMs on the inner edge of the panel, freeing up space in the detector, and simplifying any maintenance that may be required. The configuration of the newly designed outer HCal tiles mounted in an outer HCal segment is shown in Figure 3.2. Of course, by using one SiPM you also create much less data that must be combined when conducting physics analyses. Finally, the increased length of the single fiber in the new panel design makes the panel less sensitive to cladding light which is discussed in Section 3.2.

It is apparent from Figure 3.1 that the new fiber geometry provides a much more uniform response across the panel. The new panel possesses no dead spots, unlike the four fiber design when operating with the one SiPM.

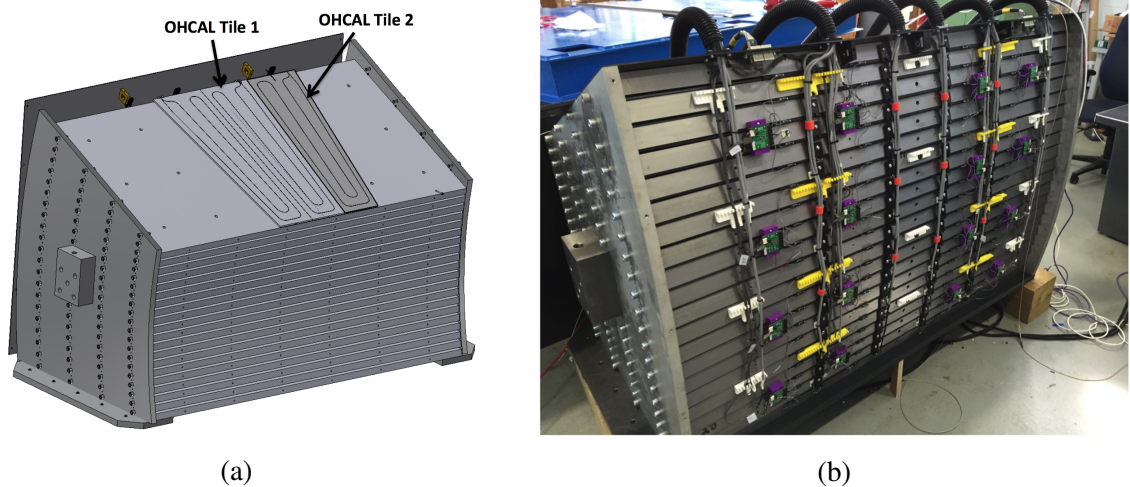


Fig. 3.2 On the left is shown a schematic diagram of the outer HCal tile designs as assembled in a segment of the HCal. Twenty steel absorber plates are separated by eighty scintillating tiles that read out their data through an SiPM on each panel on the outer edge of the segment. On the right, a photo of the outer edge of the test-beam prototype outer HCal segment with the readout electronics attached [15].

3.2 Characterizing the Amount of Light Carried in the Cladding of the WLS Fibers

One of the sources of anisotropy in the tile sensitivity is the attenuation of light trapped in the cladding of the WLS fiber. The cladding of a fiber optic cable is a layer of plastic surrounding the light carrying core of the fiber that maximizes the internal reflectivity of the fiber. The light retention capabilities of the fiber are improved by introducing a boundary between the wavelength shifting core and the surrounding material. There are fibers with multiple layers of cladding that offer better light retention at the cost of fiber durability and flexibility. Unfortunately, light can become trapped in the cladding and will remain there until it is attenuated. The cladding has a very short attenuation length that leads to light traveling in the cladding for a relatively short distance. The problem of cladding light arises from the fact that the SiPMs are mounted directly on the edge of the scintillating tiles and light that enters near the ends of the fiber will not have time to attenuate out before reaching the SiPM. The result is an artificial increase in sensitivity in the panel directly in the vicinity of the SiPM.

I investigated this effect using scans of the four-fiber tiles by calculating the signal asymmetry between SiPMs on opposite ends of the fiber as a function of position. The data taken for this study was taken using a double coincidence trigger between the two SiPMs on opposite sides of the tile. The asymmetry is defined as follows:

$$Asymmetry = \frac{yield_{right} - yield_{left}}{yield_{right} + yield_{left}} \quad (3.1)$$

I calculated the yields as seen by each SiPM by averaging the response within ± 1.5 cm of the fiber for each step in X during the scan. I chose to average the signal over each strip in X to fully capture the cladding light effect. If I had only included data from directly above the fiber, the magnitude of the asymmetry would be diminished. Additionally, the averaged response across panels is a much more relevant quantity for the development of the HCal. When sPHENIX is recording data the HCal will only report information concerning total light from each tile and sub-tile position information will not be available. In essence, all sPHENIX will see from the HCal is an averaged response from each panel. The region over which I averaged to calculate the yield from each SiPM is shown in Figure 3.3.a. The average yield is shown in 3.3.c, while the asymmetry is shown in Figure 3.3.b. I fit the yield from each SiPM independently to a simple light attenuation equation (Eq. 3.2), then I fit the asymmetry plot using that same formula. The values of the core attenuation length was taken from the manufacturer and fixed

for all the fits at $\lambda_{core} = 350\text{mm}$ [6] while the cladding attenuation length was estimated to be $\lambda_{cladding} = 5\text{mm}$.

$$I(x) = I_{core} e^{-x \lambda_{core}} + I_{cladding} e^{-x \lambda_{cladding}} \quad (3.2)$$

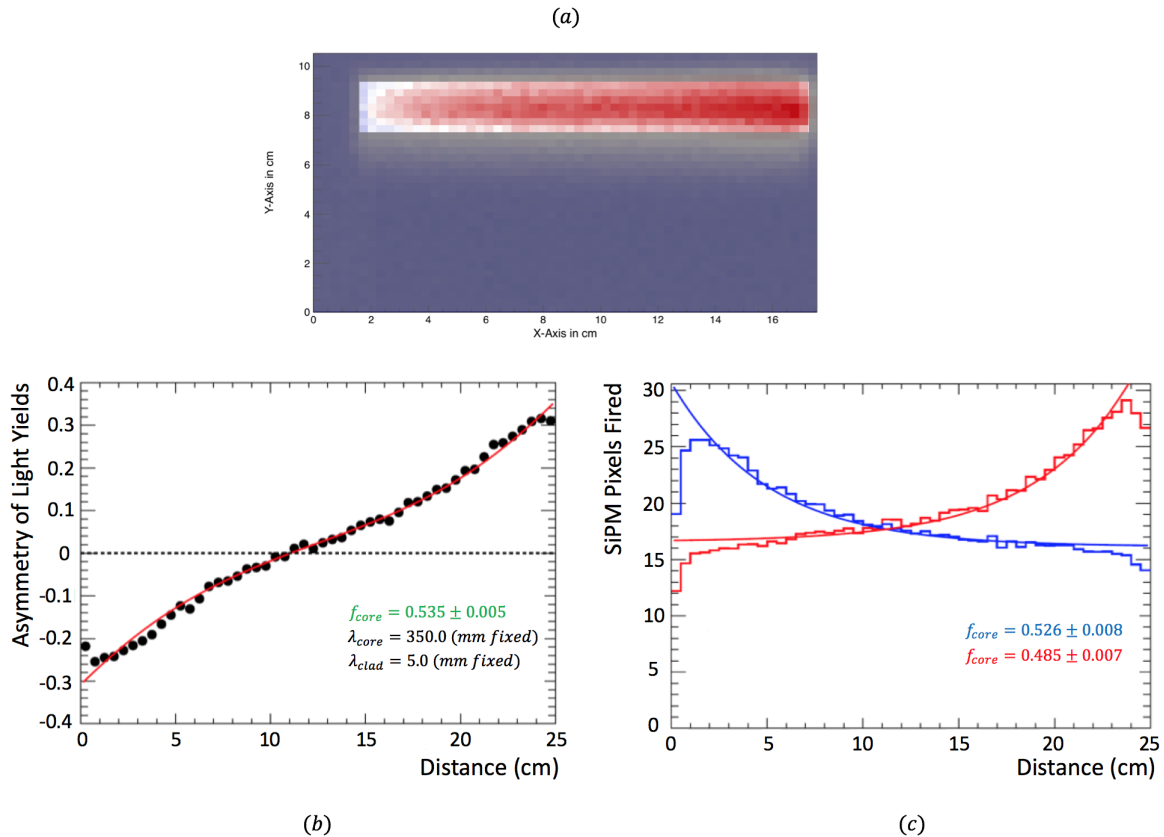


Fig. 3.3 Shown is the data I fit to determine the fraction of the light being carried in the WLS fiber's cladding. (a) I conducted a scan of an early panel design that took data from two SiPMs on opposite sides of the unbent fiber. I the average the light response within ± 1.5 cm of the fiber (the highlighted region) for each x position. (b) I calculate the asymmetry between the two SiPM responses as described above and fit the data to extract the fraction of the total light carried in the WLS fiber's core. c) Pictured is the averaged response of the SiPM on the right of the panel (in red, averaged from histogram a) next to the response from the left SiPM (in blue who's parent histogram is not shown). I then fit each set of data independently to calculate the fraction of total light carried in the fiber's core.

The fits estimated that up to 50% of the light carried in the fiber is in the cladding. As the fiber lengthens, a smaller fraction of the fiber will be subject to this cladding light effect.

This leads to a tile response that is very uniform for ($\gg 5$ mm) from the SiPM, with a spike in sensitivity of up to 50% directly in the vicinity of the SiPM. We indirectly counter this effect by placing the SiPM on the outer edge of the HCal. There, fewer particles will deposit energy in the scintillator because the hadronic showers will have mostly been stopped before they can reach that far. Additionally, using single clad fibers in the tiles minimizes the cladding light by including less cladding for the light to be trapped in. Finally, by using the long, single fiber panel geometry, the cladding light is given plenty of distance to attenuate away before reaching the SiPM. However, completely removing this effect appears to be impossible given the current WLS fiber technologies.

3.3 The Impact of Diffusive Coating Inhomogeneity on the Uniformity of Scintillating Panel Sensitivity

The diffusive coating of the HCal tiles serves a similar purpose to the cladding on the WLS fiber. The panels are exposed to a proprietary solution of aromatic solvents that deposit a thin, opaque layer on the exterior of the panel. This layer improves the internal reflection of the panels, increasing the likelihood of energy deposited in the panel reaching the WLS fibers and the SiPM. However, if there are scratches in the coating, or areas where it was applied in a nonuniform manner, the uniformity of the panel's response will deteriorate.

At one point in the development of the HCal, we received a set of panels with varying degrees of induced trauma and manufacturing inconsistencies. This included panels that were out of spec, had epoxy (from embedding the WLS fiber) spilled on the panel face, dents, and manufacturing inconsistencies. Of these defects, the ones that produced the greatest sensitivity variations were the defects in the diffusive coating. A hole in the diffusive coating allows light to escape the panel, while an increase in the diffusive coating locally increases the panel's sensitivity. In Figure 3.4 the effect of anisotropies in the diffusive coating are shown. Figure 3.4.a shows a zoomed-in photo of a defect in the diffusive coating the worst panel tested. This defect was characterized by an increased coating thickness along the left edge of the defect, coupled to a region with a thinner section of coating. Figure 3.4.b shows the effect this defect has on panel sensitivity.

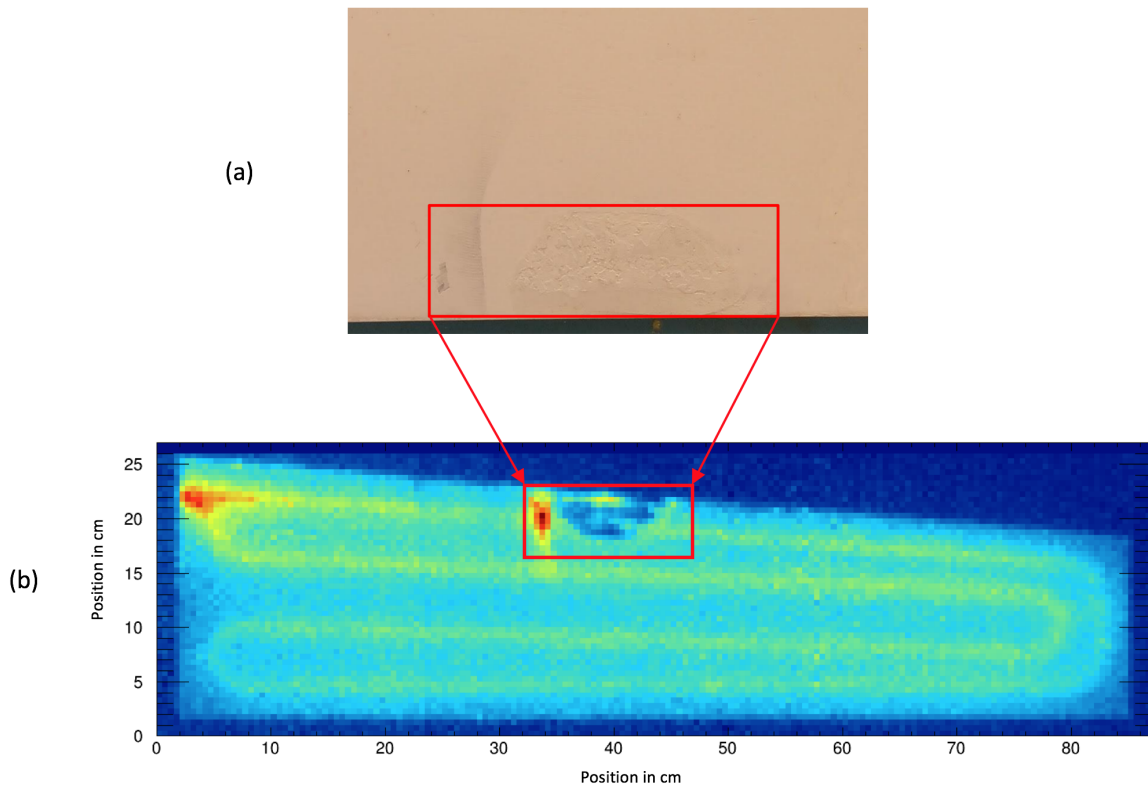


Fig. 3.4 (a) A zoomed-in photo of one of the scintillating panels we tested that had a clear aberration in its diffusive coating. (b) The LED scan of the panel pictured in (a). Upon inspection, it is clear that inhomogeneities in the diffusive coating lead to a large variation in panel sensitivity.

Luckily, detecting panels with diffusive coating anisotropies is easy because most of the time the defect is visible to the naked eye. The sPHENIX collaboration is currently in the process of deciding on how it will identify such tiles. The three options available are:

1. build an automated LED scanner that could be sent to the factory in Russia, which could provide a consistent judgment on whether a tile is sufficiently well constructed to be used in the actual experiment;
2. employ some personnel to visually inspect the panels after they have been received from the factory;
3. it may also be possible to ignore this effect because only a small fraction of the panels received from the factory had any major problems.

3.4 Results from the 2016 HCal Prototype Test Beam

The primary draw back of LED scans such as the ones I have shown in the previous sections is that the sPHENIX HCal will be detecting hadrons not LED light. Namely, before constructing the full HCal, the sPHENIX collaboration must verify the results of the LED scans using a beam of high energy mesons. To that end, a 16 GeV pion beam at Fermilab was used to make a *tile mapper* that directly verified the results of the LED scans.

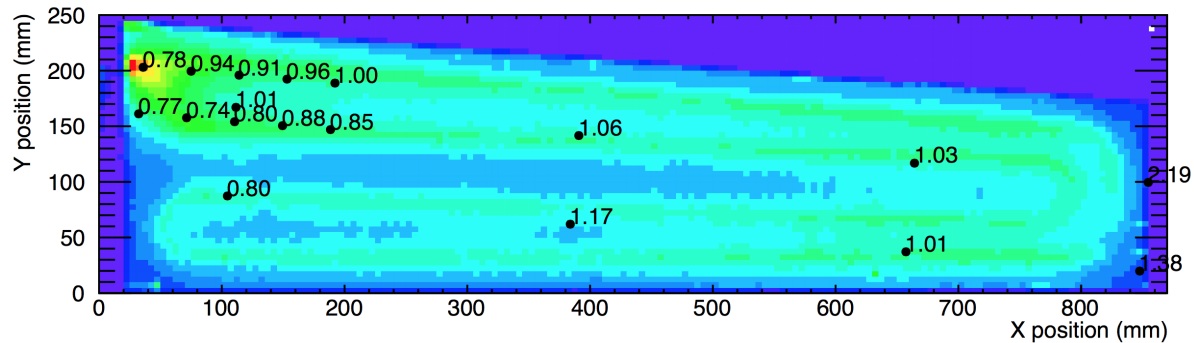


Fig. 3.5 A 495 nm LED scan with the normalized ratio of the tile mapper results over the LED data shown as the black points. The position of the black points corresponds to the actual position the 16 GeV π^- beam passed through the panel [15].

The *tile mapper* was composed of the 16 GeV π^- beam provided by the Fermilab accelerator complex and a two-dimensional motion table. Four scintillating tiles were placed on the motion table and the table was adjusted so by the end of the test, the beam had pass through the tiles at twenty different locations - ten for the outer HCal tiles and ten for the inner HCal tiles.

In Figure 3.5, an LED scan of one of the outer HCal tiles is shown with the test beam positions overlaid as black dots. The numbers next the circles report the ratio of the averaged ADC value from the 16 GeV π^- data over the average ADC value of the LED scan at that point. An arbitrary normalization was chosen so that the values of these points are approximately unity [15]. Nearly all of the points far from the SiPM show great agreement with the LED scan data. The signal from the test beam data grows less rapidly than the LED data near the SiPM. Indicating that the hot spot seen directly in front of the SiPM is less pronounced in the 16 GeV π^- data. The lower set of five test beam points are systematically lower than their LED counterparts because those point are directly on a fiber. The light deposited directly into the fibers in the LED scans makes those regions of the panel much brighter than the scan points displaced from the fiber.

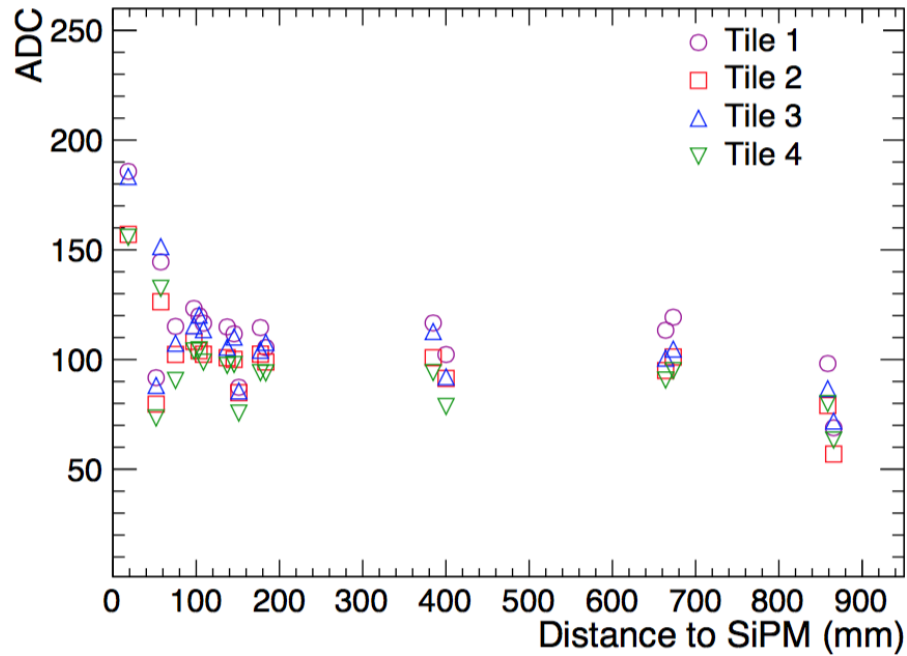


Figure ?? shows the response of the four outer HCal tiles that were tested with the 16 GeV π^- beam without comparison to the LED scans. The figure shows a uniform response within each panel for points further than 150 mm from the SiPM. However, the response starts to rise dramatically within 150 mm from the SiPM. This rise in response is due to the presence of cladding light, which as discussed in Section 3.2 is impossible to fully eliminate. Overall, the data taken during the 2016 test beam is in good agreement with the data from the LED scans I carried out. I do not show the results from the full EMCAL and HCal tests, but the detectors performed admirably and performed in agreement with simulations predicting the detectors' combined performance.

3.5 Conclusion

Over the course of the past two years I have attempted to remove sensitivity anisotropies in the scintillating tiles that will be used for the hadronic calorimeter in the sPHENIX experiment. This investigation has shed light on the impact fiber geometry has on the light response in the panel, concluding that energy deposited more than two centimeters from a wavelength shifting fiber is unlikely to be seen by the SiPM at the fiber exit. This was incorporated in the current HCal panel design resulting in a vast improvement over the previous design. Second,

the increase in panel sensitivity within 1.5 cm from the SiPM was investigated and ultimately attributed to light being carried in the cladding. While this effect could not be removed entirely, its effect was minimized by shifting away from multi-clad fibers and utilizing single-clad fibers. Finally, I characterized the effect that inconsistencies in the manufacturing of the tiles had on the panel's sensitivity. Variations in panel thickness and fiber depth were found not to impact the panels' performance; however, inconsistencies in the thickness of the diffusive coating produced massive variations in sensitivity.

Several future experiments would help to resolve some of the questions that are currently unanswered. Namely, efforts could be made to further minimize the effect of the cladding light. This could include reducing the diffusive coating in the region directly affected by the cladding light. One can also imagine investigating if the cladding light effect could be removed by sanding off the cladding at the very end of the fiber or painting an opaque circle on the end of the fiber to cover the cladding. The best way to eliminate panels containing defects in the diffusive coating is still under discussion with various options being explored that could be implemented in Russia where the panels are produced or in the USA where the detector is assembled.

Chapter 4

Methods in Developing the Double Event Algorithm for PHENIX

4.1 Detecting Double Events

I develop an algorithm to flag events with multiple interactions by examining the time dependence of data from the two Beam-Beam Counters – detectors surrounding the beam pipe on opposite ends of the interaction region, providing coverage for $3.1 < |\eta| < 3.9$. Each BBC is an array of 64 PMTs arranged radially surrounding the beam pipe at each end of PHENIX that detects the time each tube is hit by a particle and integrates the charge deposited. The algorithm I developed weights the PMT time distribution of one bunch crossing by the charge detected and looks for two independent signals. The algorithms are tested with data, in which events with double interactions are artificially produced using data from a low collision frequency run.

Event pile up is a problem all collider experiments must learn to account for if they are to take meaningful data. Many experiments rely on a silicon vertex tracker directly surrounding the interaction region to identify multiple primary vertices within one bunch crossing. This method, however, is vulnerable to several effects. First, high energy collisions produce a large number of particles at very high energies that pass expand out from the interaction region to the outer edges of the detector. Over an experiment's full lifetime, billions of such events can degrade the silicon by punching holes in the detector. Eventually, given enough radiation damage a silicon tracker can even be made obsolete. The second reason solid state tracking detectors are not ideal for identifying double events is that these detector's are difficult to make and cost a great deal of money. This results in silicon vertex tracking detectors having a comparatively small coverage

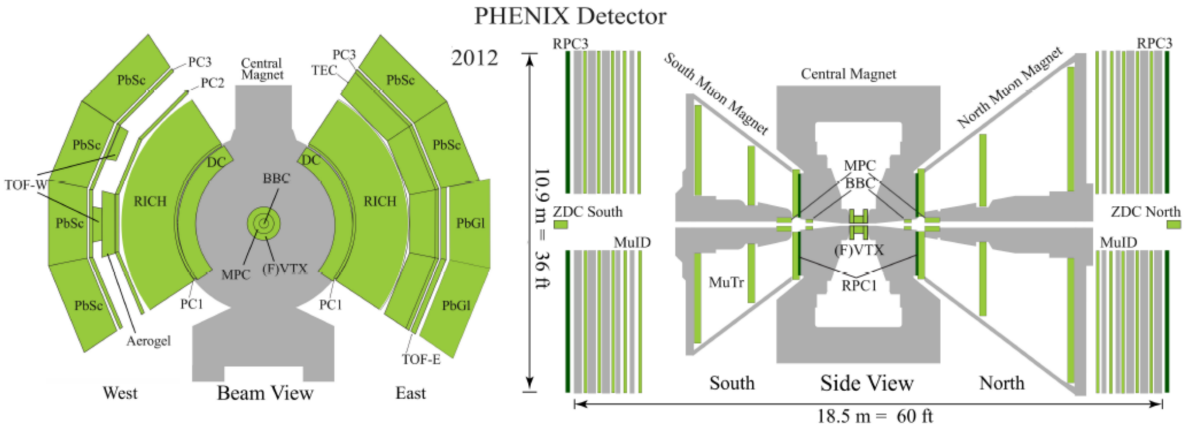


Fig. 4.1 A beam view and side view of the PHENIX experiment with the BBC positions labeled [2].

($z = 0 \pm 10$ cm in PHENIX) compared to the overall length of the experiment. One can easily imagine a double event where both events lie at opposite ends of the interaction region but their averaged position appears to be at the center of the experiment. The double event algorithm I develop does not rely on delicate silicon vertex detectors with restricted coverage and will work as long as the experiment is equipped with spectator ion counters at opposite ends of the interaction region.

4.2 Creating and Characterizing Double Events

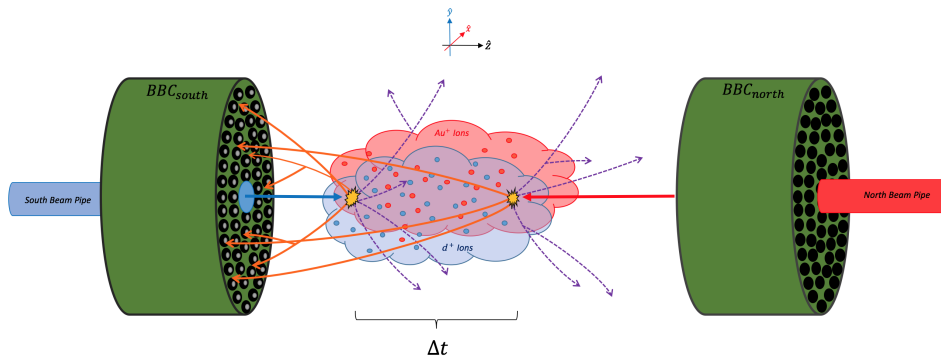


Fig. 4.2 A side view of a double event in the PHENIX detector. The algorithm calculates a Δt (ns) based on the spatial separation between events along the beam direction.

Creating an algorithm that can identify double events requires understanding all of the information available during a double event. The North and South BBCs only record two quantities - the time each PMT fires and the total charge the PMT detects over the course of the event. These two quantities define the centrality and vertex of single events. However, the meaning of an interaction's centrality and vertex is less apparent when considering a double event.

We expect the rate of double events to scale with the collision frequency of the run in question. Runs with a higher collision frequency have a greater number of ions per bunch, which leads to a higher probability for multiple nuclei to collide each bunch crossing. I combine 350 KHz data, one of the lowest collision frequencies available from the 2016 $d+Au$ run at 200 GeV, to create artificial double interactions. By inspecting these artificial doubles, I identify characteristics of double events that can be used as the basis for the algorithm. After selecting two, separate, single events, mixing requires four steps:

1. integrate the total charge from each single event as seen by the north and south BBC;
2. compare the times of the identical PMT's in each BBC fired for the two single events and record the earlier time because the BBC PMTs do not have time to reset in a single bunch crossing at PHENIX;
3. recalculate the z_{vtx} using a method similar to the online trigger used by PHENIX during a run;
4. perform cuts on the newly manufactured double event.

4.2.1 Charge Mixing

The BBC detectors at PHENIX record the total charge deposited in their PMT arrays over the course of one bunch crossing. This means that to create a realistic double event, one must add together the charge detected in each single event for each PMT. I required my manufactured double events to be among the 5% most central events for $d+Au$ collisions at 200 GeV, which corresponds to a $\Sigma Q \geq 62(q_e)$. I performed this cut on events because the initial analysis for which this algorithm was intended was investigating very central events. I show the distribution of the centralities of each single event whose combination produces a double event in the 0-5% centrality bin in Figure 4.3.

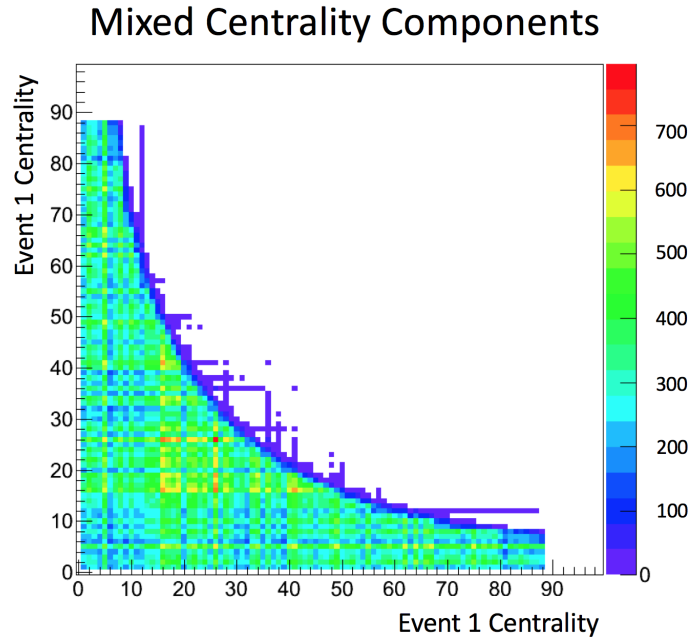


Fig. 4.3 I plot the centrality of each individual event (x and y on the plot), which is mixed to create an artificial double event. The color scale indicates the number of pairings that satisfied the $\Sigma Q \geq 62(q_e)$ cut. Surprisingly, mixed events are not substantially more likely to be created by peripheral events than they are to be created by a single central event and secondary peripheral event.

4.2.2 BBC PMT Time Mixing

Once a PMT in either BBC is fired, that specific PMT does not have enough time to reset before the ion bunches have finished passing through each other. Therefore, when manufacturing double events, one must compare each PMT's data from the two single events and record the earlier of the two times if that tube fired at all in each event. If PMT n fired at $t = 10$ ns for the first single event, but that same tube fired at $t = 15$ ns for the second single event, only $t = 10$ ns would be recorded as the time PMT n fired in the mixed event. This has the effect of biasing double events towards having prominent early time peaks and suppressed secondary peaks.

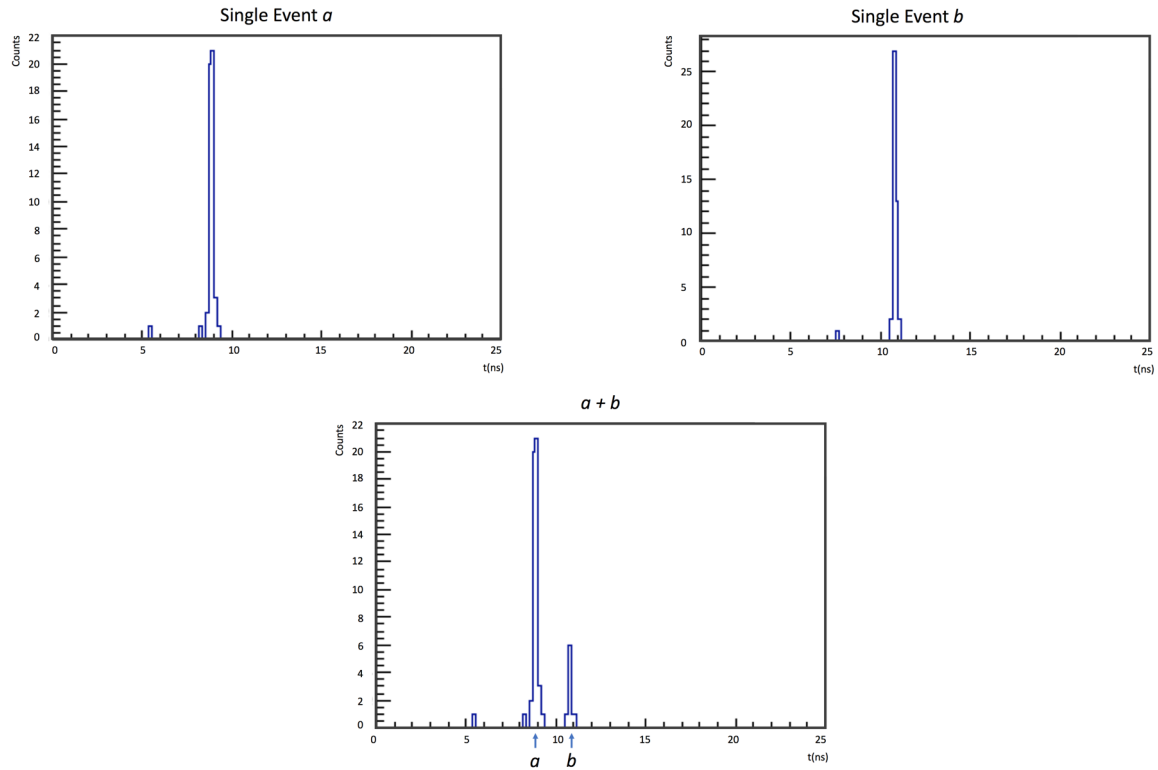


Fig. 4.4 I plot the BBC_{south} timing distributions for two single events selected from the 200 GeV $d+Au$ run at 350 kHz. Note how the position of each single event peak remains unchanged by the mixing procedure, with the only effect being the suppression of the peak in event b .

4.2.3 Vertex Mixing

The vertex of each collision at PHENIX is calculated twice—once for triggering purposes immediately before an event has been recorded, called the online z_{vrtx} , and again when the run goes through production, called the offline z_{vrtx} . The offline z_{vrtx} is a more accurate calculation of the z_{vrtx} , but is a more complicated calculation. The online z_{vrtx} , however, is a simpler calculation and provides a sufficiently accurate z_{vrtx} for the purposes of this analysis.

After the single events have been mixed to create an artificial double event, I recalculate the online z_{vrtx} by taking the average BBC PMT time for the north and south BBCs and taking the difference between them. This gives a displacement from the center of the detector in either direction along the beam path.

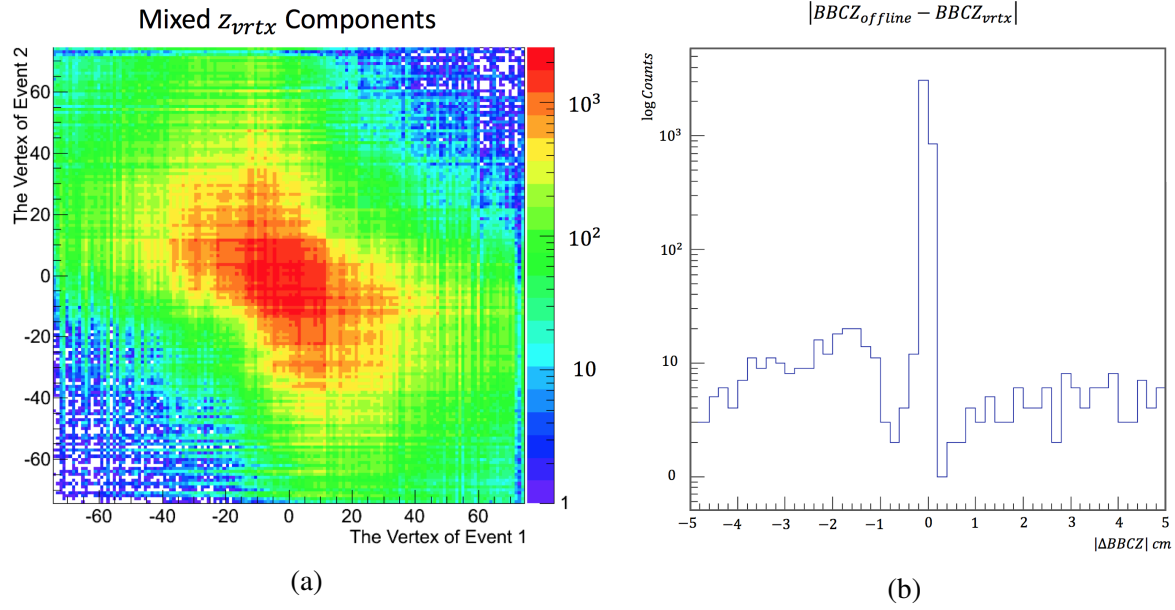


Fig. 4.5 (a) I plot the vertexes of the single events taken from the 200 GeV $d+Au$ run at 350 KHz that were used to create double events with $|z_{vrtx}| \leq 10$ cm. (b) For a sample of single events, I calculate $z_{vrtx} = [\overline{t_{BBC_{south}}} - \overline{t_{BBC_{north}}}] \frac{c}{2}$ and take its difference with the official online z_{vrtx} . This simple method of calculating the vertex clearly works with millimeter accuracy.

$$z_{vrtx} = [\overline{t_{BBC_{south}}} - \overline{t_{BBC_{north}}}] \frac{c}{2}, \quad (4.1)$$

I require the artificially mixed events to satisfy $|z_{vrtx}| \leq 10$ cm. This vertex requirement is common across most PHENIX analyses because precise tracking is only available in this z_{vrtx} range. Figure 4.5a illustrates the distribution of the single event z_{vrtx} who's combination satisfies this cut, while 4.5b verifies that the simple z_{vrtx} calculation agrees well with the offline calculation with grass that comprises $< 1\%$ of events.

4.3 Double Event Detection Algorithm

I began by studying the double event algorithm that had been conceived by the PHENIX collaboration, which provided the inspiration for looking at the timing distributions in the BBC detectors. This algorithm finds the mode of an event's time distribution across the PMTs in the BBC-south and integrates the number of tubes that fired within ± 0.5 ns of the mode. This fraction is compared to the total number of tubes that fired in the whole event to characterize

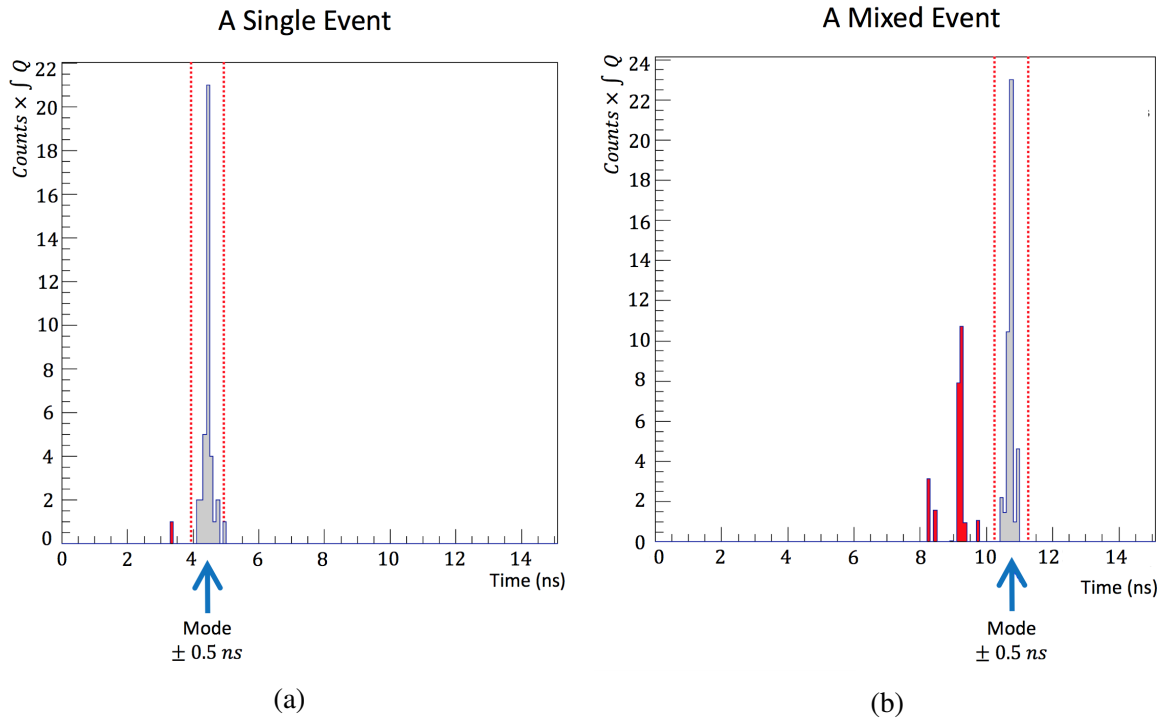


Fig. 4.6 (a) An example of a charge-weighted BBC-south PMT timing distribution for a single event, note how narrow the signal peak is. (b) An example of a charge-weighted BBC_{south} PMT timing distribution for an artificially mixed event, note how there are two, clear peaks.

the spread of PMT time signals. The algorithm relies on double events being separated by more than 0.15 meters along the beam direction. Therefore, double events occurring very near to each other in the interaction region will not be sufficiently separated in time to effectively be detected with this method.

This ratio of charge weighted counts within ± 0.5 ns of the mode to integral of the whole distribution is called the *frac*. Cutting on a given *frac* value will remove double events with a certain efficiency at the cost of unavoidably removing a small percent of one's true single events. The performance of the algorithm, along with an overview of additional uses for *frac* distributions can be found in the results section.

Chapter 5

Results from the Development of the Double Event Detection Algorithm

The primary goal of this algorithm was the detection of event pile up for the PHENIX experiment, so that double events could be cut from the analyses of interest. My primary intent when conducting this analysis was to eliminate event pile up in d+Au events at 200 GeV from Run 16. While accomplishing this goal, I found that the algorithm provided a remarkable amount of utility beyond its intended purpose. In the following sections I present the performance of the algorithm for the d+Au collision system it was developed for, but I also show how the algorithm can be used to calculate double event populations as a function of centrality and as a function of collision rate.

5.1 Removing Double Events

I have applied the algorithm to the Run 16 200 GeV d+Au data and investigate its performance. I calculate the acceptance fractions by filling separate histograms with the *frac* distributions for single and double events. Then for a given *frac* value, I integrate the histograms over the appropriate range to get the number of events that have a *frac* greater than the cut value. This is divided by the integral of the full *frac* histogram to give the fraction of events passing that cut. Single events are expected to have an acceptance fraction very close to unity, while double events should have a acceptance fraction closer to zero. In Figure 5.1 the acceptance fraction as a function of a *frac* cut is shown separated into six different centrality bins. The response is further summarized in Table 5.1 where the single event acceptance fraction and the double

event rejection fraction is shown for a $frac$ cut of 0.95. We expect even the lowest collision rate data to contain some small fraction of single events. Due to this, we expect that single event acceptance should decrease a small amount as a function of $frac$ cut. The manufactured double events should be rejected at a much higher rate, such that for a high enough $frac$ cut value the majority of manufactured double events are rejected; simultaneously, all but a small fraction of single events should pass the same $frac$ cut.

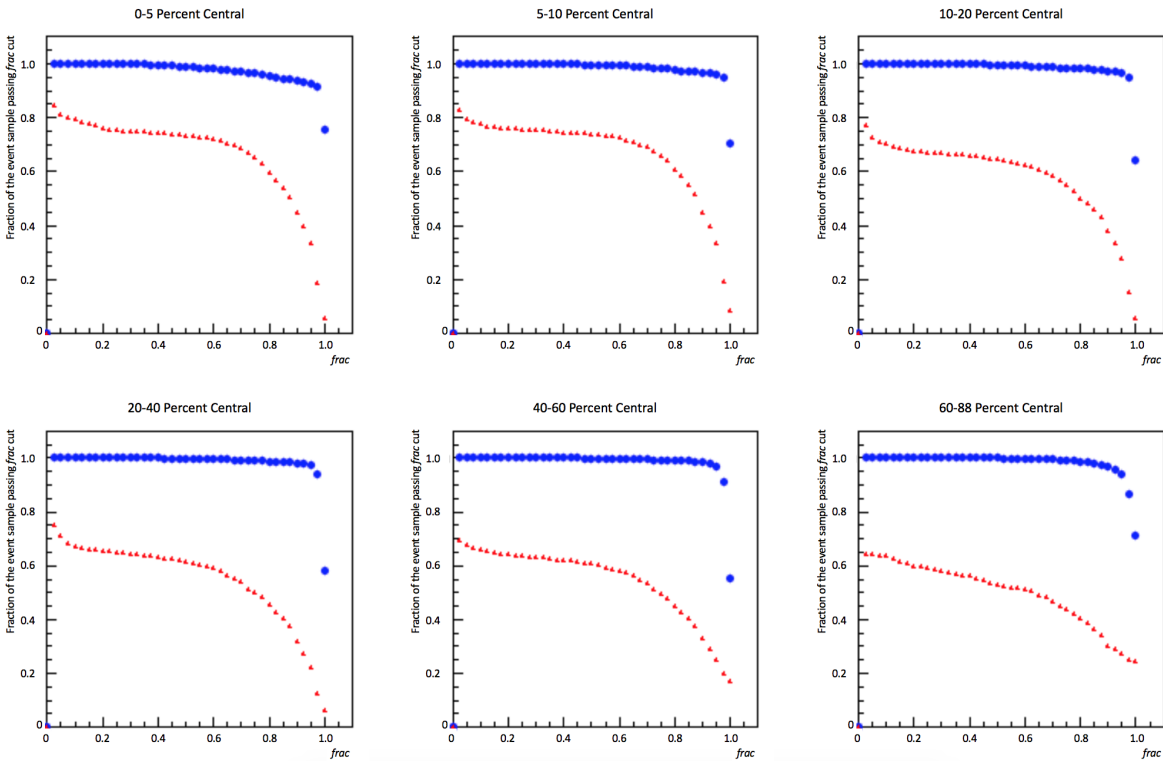


Fig. 5.1 The percentage of 350 KHz d+Au events at 200 GeV that pass a given $frac$ cut for six different centrality bins.

I found that requiring $frac > 0.95$ provided the best compromise between rejecting the majority of double events while not eliminating too many single events. This method of cutting on $frac$ values can be seen to work well in most centrality bins, but this method appears to break down for the most peripheral collisions. It is important to understand that removing double events from the sample is good, but if too many single events are removed with the double events one can hurt the available statistics enough that it is no longer worth while to make that cut. Therefore, it is necessary to further investigate the centrality and collision frequency dependence of double event populations.

Table 5.1 The fraction of double interaction events in 350 kHz data, as well as the single event acceptance fraction and double event rejection fraction, as a function of centrality. (†) The fit in the most peripheral bin is not good, and so is not reported here. The fraction is expected to be $\sim 1\%$.

	fraction of double events at 350 kHz	single event acceptance fraction ($frac > 0.95$)	double event rejection fraction ($frac < 0.95$)
0-5%	0.104	0.93	0.81
5-10%	0.058	0.95	0.83
10-20%	0.034	0.95	0.85
20-40%	0.025	0.94	0.84
40-60%	0.018	0.92	0.81
60-88%	†	0.87	0.73

5.2 Calculating Double Event Populations as Function of Centrality

Double events will typically produce more final state charged particles than their single event counterparts. Therefore, we expect that fraction of double events in a sample will decrease with increasing centrality - biasing central events to contain the most double events. I investigated this by plotting the *frac* distributions for single and double events as a function of centrality. Then for each centrality bin I scaled the double event *frac* distributions to match the single event *frac* distributions over $0.0 \leq frac \leq 0.85$. The principle behind this is that even my single event sample has some amount of real double events in it and that this double event population will define the low *frac* portion of the *frac* distributions. Therefore, by scaling the manufactured double event distribution to match over this region, one can identify if their shapes are similar. If they are, it is clear that there is a sample of real double events in the single event sample. Additionally, by taking the ratio of the integral for the scaled double event histogram to the integral of the unscaled single events, one may calculate the fraction of double events present in real data for each centrality. The results of this process are shown in Figure 5.2 and I report the ratio of the double and single event in each centrality bin as F given by:

$$F = \frac{DE_{scaled\ integral}}{SE_{integral}} \quad (5.1)$$

Figure 5.2 shows that double events are biased towards towards more central events, as expected. As usual, the double event algorithm that relies on separate peaks in the BBC time

distributions (section 4.3) struggles in the most peripheral events where there are not enough signals to form a clear peak.

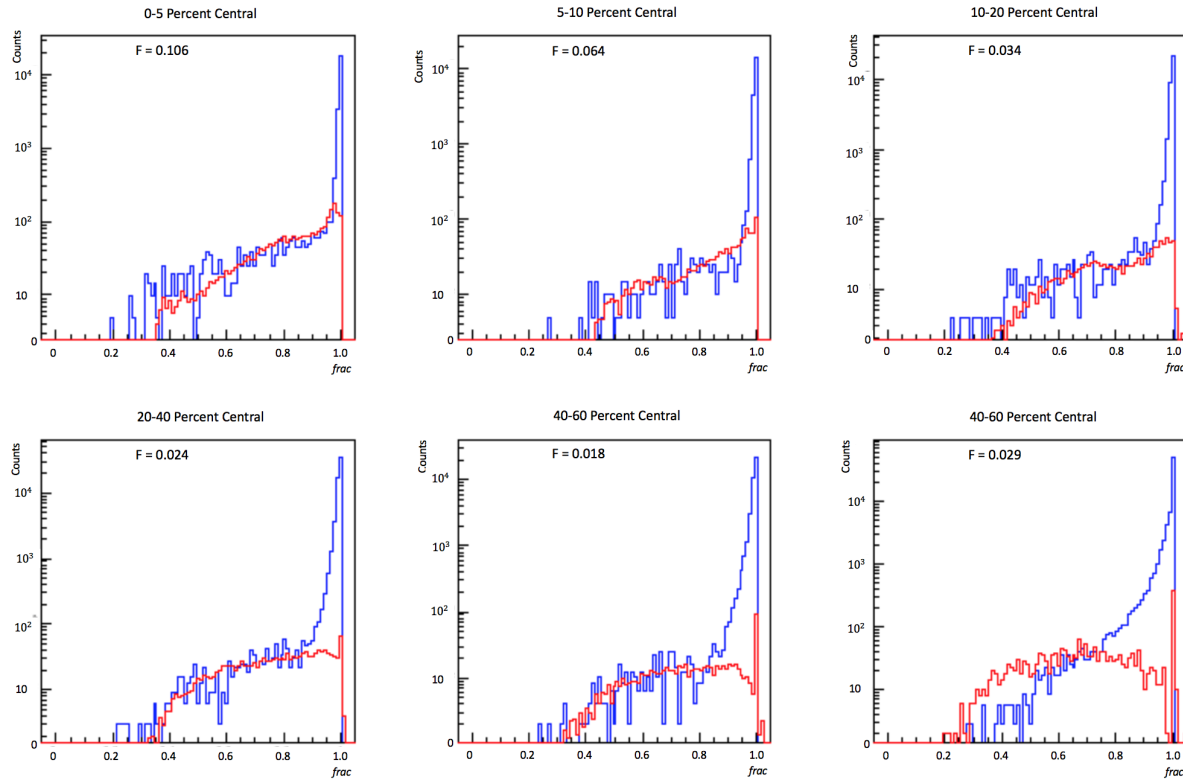


Fig. 5.2 In blue, the histograms with the *frac* distributions as calculated for 350 KHz d+Au events at 200 GeV are shown as a function of centrality. In red, the *frac* distributions for the mixed events I created are shown, where the integral of the curve over $0.0 \leq \text{frac} \leq 0.85$ has been scaled to match the integral of the blue curves. My estimate of the fraction of double events in the 350 KHz data is shown at the top of each histogram and is calculated as described above. Note that this method of estimating double event populations begins to break down for the most peripheral events (60-80% central).

5.3 Calculating Double Event Populations as Function of Collision Rate

One may use the double event detection algorithm to generate *frac* histograms that can be fit to estimate the population of double events. The result of doing this for all of the collision frequencies available from the run 16 200 GeV d+Au data is shown in Figure 5.3.

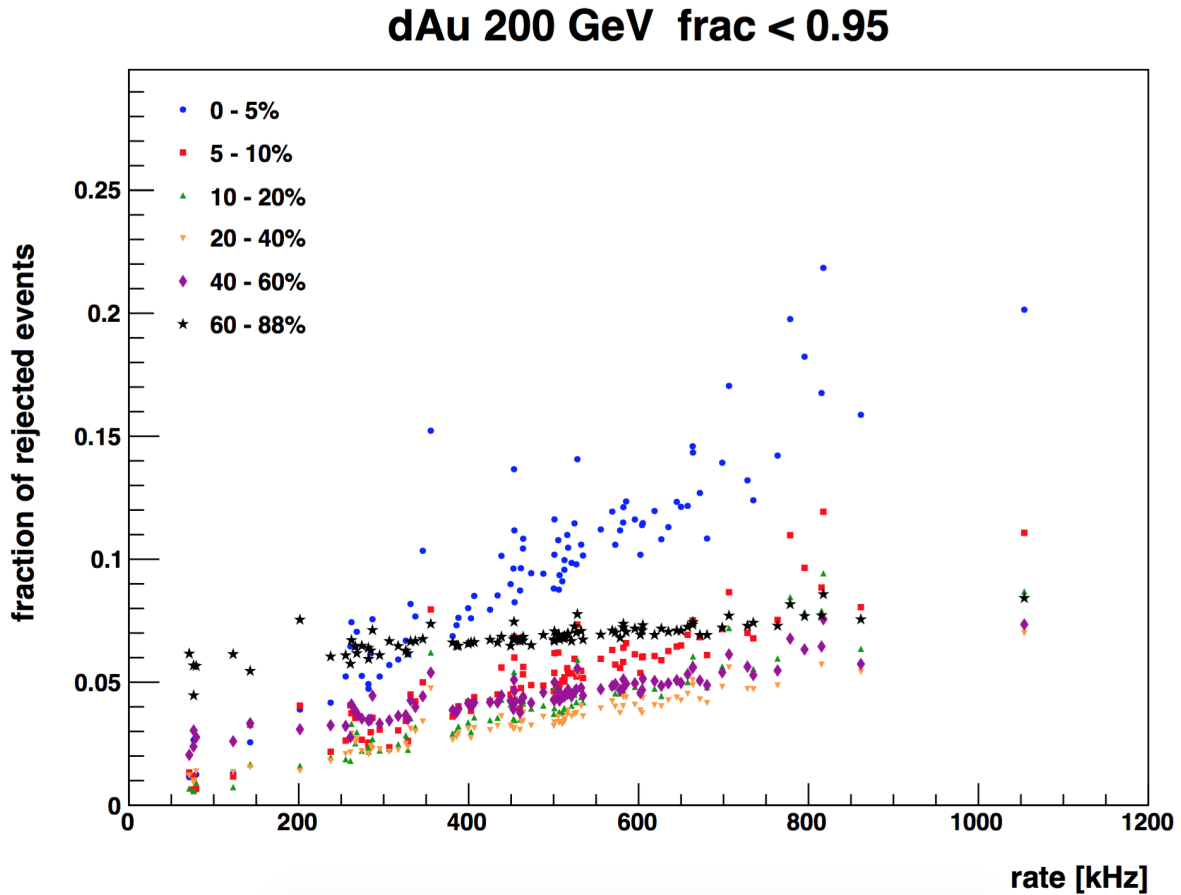


Fig. 5.3 The fraction of rejected events from various runs of d+Au at 200 GeV as a function of the run's collision rate. The various centrality bins are shown as different marker styles. The expected increase in double event populations as the collision rate increases can be seen in all but the most peripheral collisions (60-80% central).

In reality, 350 KHz is not lowest collision frequency of the 200 GeV d+Au data from run 16, there are several data sets at lower frequencies. These samples were not used in constructing the mixed events because there was a great deal more data available at 350 kHz and the properties of data at this frequency are well understood. Regardless, the algorithm can be applied to data at any frequency as shown. We expect the event pile up rate to scale as:

$$\text{double event \%} = \frac{\text{frequency}}{9.6 \text{ MHz}} \quad (5.2)$$

The double event detection algorithm now provides an alternative to this equation that was the standard within the PHENIX collaboration for estimating the rates of double events. Now,

we can derive new formulas giving the rate of event pile up as a function of collision frequency that are specific to the collision system and the centrality. For example if we perform a linear fit for each centrality class in Figure 5.3, we can estimate that for d+Au at 200 GeV the population of double events will be given by:

$$\text{double event \%} = C_{Enhancement} \frac{\text{frequency}}{9.6 \text{ MHz}} \quad (5.3)$$

$C_{Enhancement}$ is a correction taken from the linear fits of Figure 5.3 applied to the original equation to describe the distribution of event pile-up as a function of centrality. The $C_{Enhancement}$ values corresponding to each centrality are given below.

Centrality	$C_{Enhancement}$
0-5%	1.88
5-10%	0.97
10-20%	0.80
20-40%	0.59
40-60%	0.45
60-80%	0.25

Finally, this algorithm could even be used to double check the claimed collision frequency within the PHENIX collaboration. This would certainly not be the best method for calculating the collision frequency, but, never-the-less provides a quick rate sanity check.

5.4 Conclusion

I developed an algorithm to identify event pile-up in d+Au events at 200 GeV at PHENIX using the beam beam counters at opposite ends of the interaction region. Over the course of the creation of this algorithm, I manufactured fake double events using data from a low collision frequency run. I added their charges, mixed the times that the PMTs in the BBC_{south} fired, and recalculated the combined event's vertex using the same technique as the online z_{vtx} . Then I created charge wighted histograms containing the times at which the PMTs in the BBC_{south} fired and identified peaks in the distribution. Events with multiple significant peaks corresponded to events with low $frac$ values and this correlation allowed the algorithm to cut these double events from the sample. I also applied the algorithm to characterize the dependence of event pile-up on centrality and collision frequency. In the process, I developed closed form expressions to

estimate the rate of double events as a function of centrality and collision frequency for d+Au events at 200 GeV without needing to implement the algorithm.

Going forward, the algorithm could be applied to other collision systems and energies to investigate the presence of double events outside of d+Au at 200 GeV. In its current state, the algorithm performs admirably, but still fails to identify a small portion of real double events and cuts out a small fraction single events. The next logical step would be to try and incorporate information from other detectors to further refine the algorithm's accuracy. This could include trying to use the existing vertex detector's limited information somehow or even comparing the number of spectator ions to the total charged particle multiplicity.

References

- [1] A. Adare et al. sphenix, an upgrade proposal from the phenix collaboration. *arXiv:1501.06197*, 736, 2015.
- [2] C. Aidala et al.
- [3] S. Campbell. sphenix: The next generation heavy ion detector at rhic. *arXiv:1611.03003v1*.
- [4] M. Connors. Fulfilling the rhic mission with sphenix. *Journal of Physics: Conference Series*, 736, 2016.
- [5] Hamamatsu Corporation. Opto semiconductor handbook, ch 3, 2013.
- [6] Kuraray Corporation. Wavelength shifting fibers, 2016.
- [7] G. Knoll. *Radiation Detection and Measurement*. John Wiley and Sons, Hoboken, NJ, 2010.
- [8] US Department of Energy. Reaching for the horizon. *The 2015 Long Range Plan for Nuclear Science*, 1, 2015.
- [9] C. Patrignani and others (Particle Data Group). *The Review of Particle Physics*. Phys. C, Regents of the University of California, 2016.
- [10] D. Perepelitsa et al. Centrality-dependent modification of jet-production rates in deuteron-gold collisions at $\sqrt{s_{NN}} = 200\text{gev}$. *Phys. Rev. C*, 94, 2016.
- [11] G. Pinholster. Evidence shows that cosmic rays come from exploding stars. *Science*.
- [12] RHIC. The physics of rhic, 2016.
- [13] S. Seeds. Equalizing photoelectron response across scintillators employing wavelength shifting fibers. Master's thesis, University of Colorado at Boulder, 2014.
- [14] M. Thompson. *Modern Particle Physics*. Cambridge University Press, Cambridge, UK, 2013.
- [15] S. Vazquez-Carson et al. Beam test results for the sphenix electromagnetic and hadronic calorimeter prototypes. *IEEE Transaction on Nuclear Science (In Preparation)*.
- [16] W. Zajc et al. The first few microseconds. *Scientific American*, pages 34–41, 2006.